Resolved DEM-CFD coupling for wave-armour blocks interactions

Matthieu Barcet, William Benguigui, Jérôme Laviéville, Michel Benoit, Anthony Wachs, Pascal Fede, Thomas Bonometti

Resolved DEM-CFD Coupling for Wave-Armour Blocks Interactions

Matthieu Barcet[a,b], William Benguigui[a,c,*], Jérôme Laviéville[a], Michel Benoit[d,e], Anthony Wachs[f,g], Pascal Fede[b] and Thomas Bonometti[b]

[a] EDF R&D, Mécanique des Fluides, Energie, Environnement (MFEE), 6 quai Watier, 78400 Chatou, France
[b] Institut de Mécanique des Fluides de Toulouse (IMFT), Université de Toulouse, CNRS, INPT, UPS, 31400 Toulouse, France
[c] IMSIA, UMR 9219 EDF/CNRS/CEA/ENSTA, 828 Bd des Maréchaux, 91120 Palaiseau, France
[d] EDF R&D, Laboratoire National d'Hydraulique et Environnement (LNHE), 6 quai Watier, 78400 Chatou, France
[e] LHSV, Saint-Venant Hydraulics Laboratory, ENPC, Institut Polytechnique de Paris, EDF R&D, 6 Quai Watier, 78400 Chatou, France
[f] University of British Columbia, Department of Mathematics, 1984 Mathematics Road, Vancouver, BC V6T 1Z4, Canada
[g] University of British Columbia, Department of Chemical and Biological Engineering, 2360 East Mall, Vancouver, BC V6T 1Z3, Canada

ARTICLE INFO

Keywords:
Wave structure interaction
DEM-CFD Coupling
Discrete forcing method
Breakwater stability
Experimental wave load

ABSTRACT

The present work aims to tackle breakwater stability challenges through an innovative numerical deterministic method using a resolved DEM-CFD (Discrete Element Method – Computational Fluid Dynamics) strategy, which simulates the individual motions of armour units within a fluid solver. To achieve this, a coupling between a DEM code and a CFD code is implemented and validated. The fluids (air and water) are solved using a Eulerian-Eulerian CFD solver, and the contacts between blocks are solved using a DEM code. The solids are defined within the fluid solver using a discrete forcing approach and are therefore fully resolved. In this way, the fluid solver enables the prediction of object motions with complex shapes such as tetrapods. To couple the codes, forces exerted on the solids are calculated in the fluid solver and sent to the DEM solver. Then, contact and gravity forces are computed and added to the fluid forces. The DEM solver then computes the new positions and velocities of the bodies, which are retrieved by the fluid solver. An experimental study is performed on a fixed and instrumented idealized breakwater to evaluate the wave forces acting on a coastal structure. The experiments are then numerically reproduced to validate the numerical model. Simulations of the impact of solitary waves on a row of mobile isolated tetrapods laid on a horizontal berm are then performed using the DEM-CFD coupling. The importance of initial placement and friction parameters is investigated to show the sensitivity to these parameters.

1. Introduction

The stability of rubble mound breakwaters is a critical issue for coastal and harbour protections. The armour layer is made of concrete units or quarried rocks and plays a key role in the breakwater integrity. It protects the filter layers and the core of the dike by dissipating the wave energy and by limiting the internal displacement of material. However, degradation of the armour layer can occur when the wave load is significant by breaking or displacing armour units, jeopardizing the integrity of the core and reducing the efficiency of the breakwater. Critical failures are rare but can have serious impacts on the coastal infrastructure. Such failures occurred for example at Sines, Portugal (1978), Arzew El Djedid, Algeria (1980), and Crescent City, California (1983) (Baird et al. (1980), Burcharth (1987), Scaravaglione et al. (2022), Jensen (2024)). Breakwaters stability is generally estimated using semi-empirical design formulas based on experimental studies or on-site observations. The Hudson formula is the most widely known formula which has been used for several decades (Iribarren (1938), Hudson (1959), Losada and Gimenez-Curto (1979), Van Der Meer (1987), Van Der Meer (1988), USACE (2002)), Van Gent et al. (2004), CIRIA et al. (2007). In-depth studies are still performed with physical scale models in order to improve the design formulas, study specific wave cases or the effectiveness of new configurations (van Gent and van der Werf (2014), Altomare and Gironella (2014), Scaravaglione et al. (2025)). However, numerical studies have increasingly been used during the past two decades to complement the experimental studies in coastal-related research.

The interaction of waves with single moving rigid bodies has been extensively investigated over the past decades using several numerical methods. For instance, Koo and Kim (2004) applied the fully non-linear potential flow

*Corresponding author: william.benguigui@edf.fr

theory, Zhao and Hu (2012) and Zhao et al. (2014) used a CIP (Constrained Interpolation Profile) based method, Bouscasse et al. (2013) used SPH (Smoothed Particle Hydrodynamics), and Chen et al. (2016) used a CFD model with a Cartesian cutcell method. These approaches demonstrated promising results, even though the use of simple shapes and 2D domains limits their applications. More recently, the improvement of codes and methods has enabled the representations of complex shape in 3D setup and with highly non-linear and breaking waves. For instance, an extensive comparison of potential, CFD and SPH codes regarding the hydrodynamic response of a floating offshore wind turbine is presented in Yu et al. (2025). Several other studies have shown that the modeling of single floating rigid bodies is well-captured with several methods (Rongé et al. (2023) with potential flow theory and CFD, Han and Dong (2023) and Salis et al. (2024) with the SPH methods).

However, real-world coastal structures such as breakwaters are inherently multi-body systems, often composed of thousands of interlocking units. Single-body models cannot capture the structure's behavior due to inter-particle contacts. To address this, researchers have turned to either porous media approximations (Wu et al. (2014), Senturk et al. (2023)) or to the discrete modeling of individual elements. To do so, fluid codes have been coupled to Discrete Element Method (DEM) codes to represent the contacts between the objects. State of the art methods include CFD-DEM coupling, SPH-DEM coupling or Material Point Method (MPM) which are well described and compared in Bonus et al. (2025).

These fluid-DEM coupling methods are now frequently used in geophysical researches to represent submarine avalanches and landslides (Wu et al. (2018), Izard et al. (2018), Jiang et al. (2018), Bao et al. (2023)). Initially, DEM dealt with spherical particles, but non-spherical particles enabling the representation of a wider range of scenarios are increasingly used (Ma et al. (2022), Sun et al. (2023)). Furthermore, recent studies have demonstrated the potential of fluid-DEM coupling in simulating wave interaction with breakwaters. For example, Sarfaraz and Pak (2018) studied the wave impact on a 2D breakwater composed of cubic armoured blocks using a SPH-DEM coupling, with limited movement. They proposed new design formulas but highlighted the necessity to perform realistic scenarios with 3D configurations. Ding et al. (2021) explored the hydrodynamic response of a caisson-type breakwater stabilized by armour units, using a CFD-DEM coupling. However, the hydrodynamic impact is located on the caisson which then transfers its movement to the armour units. It limits the applicability of the method to specific types of breakwaters, where there is no direct wave impact on the armour units. Furthermore, Chen and Zhang (2023) and Chen et al. (2025) used a semi-resolved CFD-DEM coupling to model the interaction of waves with submerged permeable breakwaters. Wang et al. (2024) investigated the stability of Accropode-type armour units placed on a slope using a coupled CFD-DEM approach, demonstrating the viability of this method. However, for simulations involving direct wave interaction with armour units, the SPH-DEM coupling is the most used method. For instance, Mitsui et al. (2023) used a SPH-DEM coupling made by Martínez-Estévez et al. (2023) to model the wave impact of a solitary wave on a row of tetrapods. The comparison with experimental results shows the capabilities of the method in non-realistic wave-structure interaction setup. Similarly, Sun et al. (2024) studied the impact of free surface flows over breakwater type structures with non-realistic (columns of cubes) and realistic (pile of rocks randomly arranged) setups, using SPH-DEM. Recently, Bonus et al. (2025) compared several method (CFD-DEM, SPH-DEM and MPM) with experimental results to model the impact of a tsunami carrying debris into a harbour. They showed that the three methods were highly performing regarding the debris final distribution, and that the CFD-DEM code yielded the best results regarding hydrodynamic performance.

In this study, the focus is made on the presentation of a new fully resolved CFD-DEM coupling, based on a discrete forcing method (Benguigui et al. (2018), Benguigui et al. (2019)), and its application to coastal-related studies. To do so, we first present the DEM and CFD codes as well as the coupling between them in section 2. In section 3, we validate the wave modeling and show the capacity of the code to evaluate the forces of non-breaking or breaking waves on coastal protections by comparing our CFD method with an in-house experimental study. Finally, a coastal engineering related case is performed and presented in section 4. It consists in sending a solitary wave toward a row of tetrapods and studying their responses as in the experiments conducted by Mitsui et al. (2023). Furthermore, sensitivity analyses on friction parameters and initial placement of the blocks are performed and discussed.

2. Numerical Modeling

The codes used here for the DEM-CFD coupling are neptune_cfd and Grains3D. Grains3D is a DEM code capable of modeling the contacts between a high number of non-convex particles (Wachs et al. (2012), Rakotonirina (2018), Rakotonirina et al. (2019)). neptune_cfd is a multifluid Eulerian-Eulerian code that can model complex free surface

flows. Moving bodies are modeled through a discrete forcing method (Benguigui et al. (2018), Benguigui et al. (2019)) similar to an Immersed Boundary Method (IBM). It enables the simulation of wave-structure interactions, such as a wave breaking against a wall with a recurved parapet (Benoit et al., 2023), and the study of floating offshore wind turbines at a local scale (Rongé et al. (2023), Benguigui and Peyrard (2024)). To do so, fluid forces on resolved immersed bodies are computed using a direct integration of the pressure and viscous stress components at the fluid-structure interface (cut-cells), before solving the displacement and updating object positions and velocities. The coupling is made with the CFD code as the leading code, which calls the DEM code at each iteration to solve the contact forces between the rigid bodies and to determine their displacements.

2.1. Discrete Element Method

The DEM was initially developed by Cundall (1971) to describe movements in blocky rock systems. The method is based on a Lagrangian tracking of the particles and a contact modeling between particles to determine interaction forces. The DEM code used here, Grains3D, was introduced by Wachs et al. (2012) in order to simulate the flow dynamics of granular material made of non-spherical rigid particles.

To determine if two objects are in contact and to obtain the overlapping distance between them δ_n (required for the DEM forces calculations), the DEM code uses the GJK algorithm (Gilbert–Johnson–Keerthi). It was first described by Gilbert et al. (1988) as a fast and reliable way to compute the distance between complex 3D objects for robotic applications. The algorithm was popularized by the video game industry as its efficiency allows real-time resolution of object collisions for simple problems. A fast and robust implementation of the algorithm is presented in Bergen (1999). The limitation of the algorithm lies in the variety of shapes that can be described. The algorithm is indeed limited to classes of convex rigid bodies with known support functions which include convex polytopes (polygons or polyhedra), boxes, spheres, cylinders or cones. However, the convex object limitation is overcome by gluing together multiple convex particles to obtain a non-convex super-particle (Rakotonirina et al., 2019).

Once the distance algorithm has determined that two bodies are overlapping, forces are calculated to model the contact. The contact force $\vec{F}_c$ used here is divided into a normal force $\vec{F}_n$ and tangential force $\vec{F}_t$:

$$\vec{F}_c = \vec{F}_n + \vec{F}_t \tag{1}$$

The normal force is represented using a spring-dashpot model, with the following formulation:

$$\vec{F}_n = \vec{F}_{n,spr} + \vec{F}_{n,dis} \tag{2}$$

with $\vec{F}_{n,spr}$ and $\vec{F}_{n,dis}$ respectively the normal spring and dissipating components which are of type:

$$\vec{F}_{n,spr} = k_n \delta_n \vec{n} \tag{3}$$

with k_n the normal spring stiffness, δ_n the overlapping distance between the two bodies and $\vec{n}$ the unit normal vector at the contact point, and:

$$\vec{F}_{n,dis} = -2\mu_n m \vec{U}_{nr} \tag{4}$$

with μ_n the normal dissipation coefficient, m the reduced mass and $\vec{U}_{nr}$ the normal relative velocity.

The tangential force is separated into two components: a static component and a dynamic component. The static component is modeled using a spring-dashpot model, and the dynamic one follows a Coulomb type model.

$$\vec{F}_t = -\min(|\vec{F}_{t,stat}|, |\vec{F}_{t,dyn}|)\vec{t} \tag{5}$$

with $\vec{F}_{t,stat} = \vec{F}_{t,spr} + \vec{F}_{t,dis}$ the static component, $\vec{F}_{t,dyn}$ the dynamic component and $\vec{t}$ the unit tangential vector at the contact point. $\vec{F}_{t,dis}$ and $\vec{F}_{t,spr}$ can be written as follow:

$$\vec{F}_{t,dis} = -2\mu_t m \vec{U}_{tr} \tag{6}$$

with μ_t the shear dissipation coefficient and $\vec{U}_{tr}$ the tangential relative velocity.

$$\vec{F}_{t,spr} = \vec{F}_{t,spr,memory} + k_t \vec{\delta}_t \tag{7}$$

with $\vec{F}_{t,spr,memory}$ the tangential spring force at the previous time step projected on the new tangential contact plane (i.e. a memory force since the beginning of the contact). If the Coulomb limit is reached and therefore the force is of the dynamic type, $\vec{F}_{t,spr,memory}$ is recalculated to reach equilibrium (i.e. $\vec{F}_{t,spr,memory} = \vec{F}_{t,dis} - \vec{F}_{t,stat}$). δ_t is the slip in tangential direction for the current time obtained by integrating the tangential velocity over a time step and k_t is the tangential spring stiffness. The dynamic component, of Coulomb type, is written as follows:

$$\vec{F}_{t,dyn} = -\mu_c \left|\vec{F}_n\right| \vec{t} \tag{8}$$

with μ_c the dynamic friction coefficient. The physical parameters of the simulations are e_n the coefficient of normal restitution and μ_c the dynamic friction coefficient. The other parameters k_n, k_t, μ_n and μ_t are purely numerical parameters. e_n is used in the determination of μ_n to obtain the desired normal behaviour:

$$\mu_n = -\omega_0 \frac{\log(e_n)}{\sqrt{\pi^2 + \log(e_n)^2}} \tag{9}$$

with $\omega_0 = \sqrt{k_n/m}$ the natural angular frequency of the equivalent mass-spring system.

A schematic of the normal and tangential forces can be found in Figure 1. A more detailed description of the DEM forces can be found in Wachs et al. (2012) and Huet et al. (2021). The equation of motion of the particles are obtained by applying Newton's second law to each particle. The displacement and rotation are then obtained by integrating and discretizing the equation using the leap-frog Verlet scheme, a second order scheme with one force evaluation per time step, selected for its good balance between accuracy, low complexity and computing time (Džiugys and Peters, 2001).

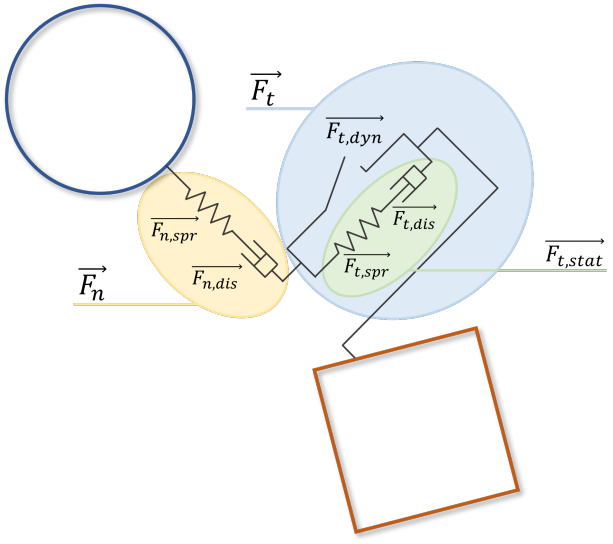

Figure 1: Sketch of the forces included in the DEM model with $\vec{F}_n$ the normal force composed of a spring component $\vec{F}_{n,spr}$ and a dissipative component $\vec{F}_{n,dis}$, $\vec{F}_t$ the tangential force composed of a dynamic component $\vec{F}_{t,dyn}$ and a static component $\vec{F}_{t,stat}$ itself made of a spring component $\vec{F}_{t,spr}$ and a dissipative component $\vec{F}_{t,dis}$.

2.2. Two-phase flow modeling

2.2.1. Eulerian-Eulerian formulation

The CMFD (Computational Multi-Fluid Dynamics) code neptune_cfd is based on a two-fluid approach (Guelfi et al., 2007). It is a finite-volume code with a collocated arrangement for all variables. A fully face-based data structure allows cells to be arbitrary shaped when building the mesh. A pressure correction approach based on Ishii (1975) is used to compute multiphase flow with a set of two conservation equations (mass and momentum since the present work is focused on adiabatic free-surface flows) for each field. The volume fractions α_k satisfy:

$$\sum_k \alpha_k = 1 \tag{10}$$

For each field k, the mass balance is written as:

$$\frac{\partial}{\partial t}\left(\alpha_k \rho_k\right) + \nabla \cdot \left(\alpha_k \rho_k \vec{u}_k\right) = \sum_{p \neq k} \Gamma_{p \to k} \tag{11}$$

with ρ_k the density of the field k, $\vec{u}_k$ the velocity of field k, and $\Gamma_{p \to k}$ the mass exchange rate between fields p and k. In the present study, no mass exchange takes place between the phases and therefore $\Gamma_{p \to k} = 0$. The momentum balance for phase k is written as:

$$\frac{\partial}{\partial t}\left(\alpha_k \rho_k \vec{u}_k\right) + \nabla \cdot \left(\alpha_k \rho_k \vec{u}_k \otimes \vec{u}_k\right) = -\alpha_k \nabla P + \alpha_k \rho_k \vec{g} + \nabla \cdot \left(\alpha_k \mu_k \left(\nabla \vec{u}_k + {}^{\mathrm{T}}\nabla \vec{u}_k\right)\right) + \sum_{p \neq k} \vec{I}_{p \to k} \tag{12}$$

with μ_k the viscosity of field k, $\vec{g}$ the gravity and $\vec{I}_{p \to k}$ representing the momentum exchange rate between fields p and k.

These equations are deduced from the volumetric averaging of local instantaneous ones. Volume fractions and velocity fields are updated using a SOLU scheme (Second Order Linear Upwind) while the pressure field is computed using the SIMPLE algorithm. Fields can represent different kinds of multiphase flows. Depending on the two-phase structures, the interfacial momentum transfers of each phase are predicted with a specific model. In this study, a turbulence model called R_{ij}-SSG is used for the liquid phase. It consists in computing a set of equations of evolution for the components of the Reynolds stress tensor and the shear stress production term used in the equation of evolution of the turbulent dissipation rate. Details can be found in Speziale et al. (1991).

2.2.2. Free surface tracking method: Large Interface Model

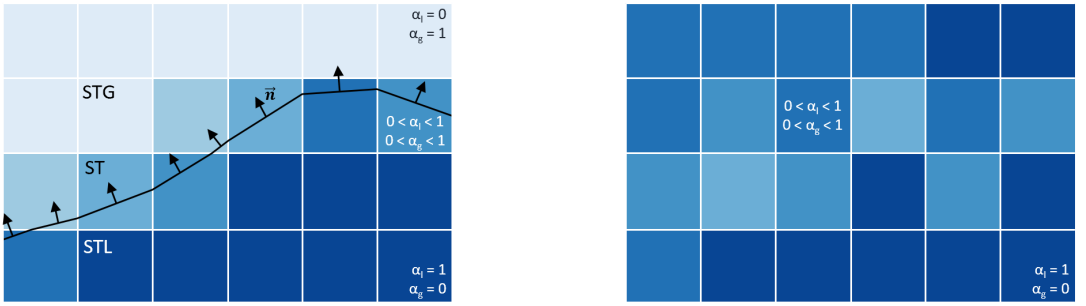

Figure 2: Schematic meshes with the liquid and gas volume fractions represented. Left: a clear delimitation can be seen and the LIM reconstructs an interface. Right: no clear interface can be reconstructed, only the classic phase dispersed modeling is used.

In order to model the interface between two phases, the Large Interface Model (LIM) is used (see Figure 2). It deals with large interfaces, i.e. much larger than the order of magnitude of a cell size. First, the interface is captured by searching for the boundary between phases. A specific treatment is then applied to the flagged cells to model the phases interactions.

To capture the interface, the LIM uses the gradient of volume fraction. When the gradient of volume fraction $||\nabla \alpha_l||$ projected in any direction exceeds a threshold value, the cell is flagged as being an interfacial cell (ST). To complete the three-cell stencil, a gas cell (STG) and a liquid cell (STL) are selected on both sides of the interface, using the normal to the surface $\vec{n} = \nabla \alpha_l / ||\nabla \alpha_l||$. Once detected, the interfacial cells receive a specific treatment to model the momentum exchange τ between the phases, separated into a tangential component τ_t and a normal component τ_n. The tangential component reads:

$$\tau_t = \rho_g (u_g^*)^2 A \tag{13}$$

with ρ_g the gas density, u_g^* the gas friction velocity at the interface determined using a wall law-like method and A an estimation of the interfacial area (in m^2) of the three-cell stencil. The continuity of shear stress across the interface

implies that $\rho_g(u_g^*)^2 = \rho_l(u_l^*)^2$ and that the frictions forces are symmetrical. The normal component of the momentum exchange follows a drag-type law in the shape of:

$$\tau_n = \alpha_l \alpha_g C_D(\vec{u}_l - \vec{u}_g) \cdot \vec{n} \tag{14}$$

with C_D the standard drag coefficient used in the dispersed phase, to ensure that the normal relative velocity between both phases tends towards 0. Further details on the LIM and on the turbulence exchange at the interface equations can be found in Coste (2013) and Coste and Laviéville (2015). In this work, the model is used to describe the free surface and allows the surface waves to propagate accurately. When the LIM is not applicable (i.e. no clear interface is detected, see Figure 2), a separated phase model is used with classical bubble and droplet drag, lift and added mass components depending on the ratio between the phases (Mer et al., 2018).

2.2.3. Solid modeling

Solid bodies are modeled with a discrete forcing method using a cut-cell strategy called Time and Space Dependent Porosity (Benguigui et al., 2018). The principle of this method is to recreate the geometry of an object directly inside cut-cells (i.e. cells on the fluid-structure interface). In the first step, the geometry is captured in a Lagrangian framework and represented with a solid fraction inside each cell, called porosity. The porosity ε of a cell is defined as:

$$\varepsilon = \frac{V_f}{V_{tot}} = 1 - \alpha_s \tag{15}$$

with α_s the volumetric fraction of the solid phase, and V_f and V_{tot} the fluid and total volumes of a cell, respectively. Equation (10) then becomes:

$$\sum_k \alpha_k = \varepsilon \tag{16}$$

Immersed structures are defined geometrically with a colour function that categorizes cells into three groups: cells with only fluid phases ($\varepsilon = 1$), cells with only a solid phase ($\varepsilon = 0$), and cut-cells partially fluid and partially solid ($0 < \varepsilon < 1$) where ε is precisely calculated using a recursive penalisation function and based on the position of the structure. A new fully fluid cell is then built in each cut-cell based on the position and motion of the structure by updating the center of gravity, the wall normal, and therefore the boundary condition. This is illustrated in Figure 3. Then, the mass and momentum balance equations are discretely corrected in cut-cells to take into account the presence of the structure and its motion.

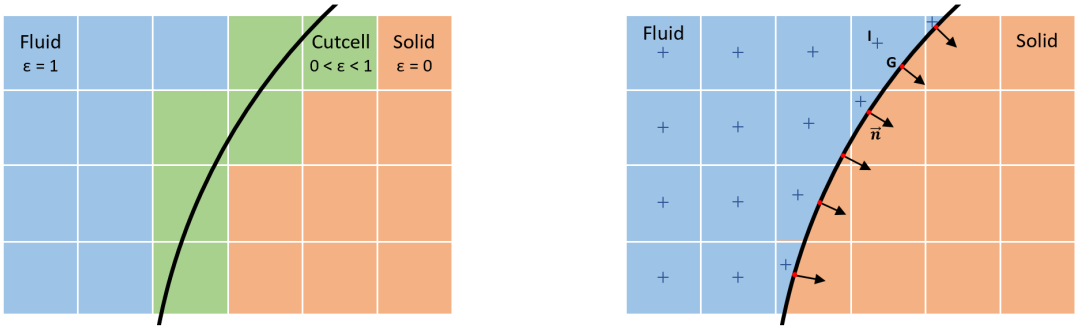

Figure 3: Mesh with part of a cylinder seen from above. Left: cells are tagged as fluid cells (blue), solid cells (orange) and cut-cells (green). Right: cut-cells are recomputed as fluid cells with a new center of gravity (I) and a new face normal ($\vec{n}$) like with a body fitted mesh.

This discrete forcing method allows the construction of complex shapes, with the possibility to impose a motion to the object. Furthermore, by calculating the forces acting on the object, its free motion can be predicted. The fluid forces $\vec{F}_f$ are obtained using equation (17):

$$\vec{F}_f = \vec{F}_{pressure} + \vec{F}_{friction} \tag{17}$$

The pressure contribution $\vec{F}_{pressure}$ is determined by explicitly integrating the pressure at the wall of the object in every cutcell (equation (18)), the value of pressure being determined by extrapolating the pressure from the reconstructed cell center of gravity I to the solid face center of gravity G:

$$\vec{F}_{pressure} = \int_{\Omega} P_G \overrightarrow{dS} \tag{18}$$

$$P_G = P_I + \overrightarrow{IG} \cdot \overrightarrow{\nabla P}_I \tag{19}$$

with P_G and P_I respectively the pressure at G and I, $\overrightarrow{IG}$ the vector from I to G and S the surface on which the pressure is applied. Similarly, the friction contribution $\vec{F}_{friction}$ is calculated using the velocity gradient computed at the wall, over every phase k:

$$\vec{F}_{friction} = \sum_k \frac{\alpha_k}{\varepsilon} \mu_k \left(\overline{\overline{\nabla u_{k,G}}} + {}^T\overline{\overline{\nabla u_{k,G}}} \right) \vec{S} \tag{20}$$

with μ_k the viscosity of field k and $u_{k,G}$ the velocity of phase k at the wall. Details can be found in Benguigui et al. (2019).

2.3. Resolved DEM-CFD explicit coupling

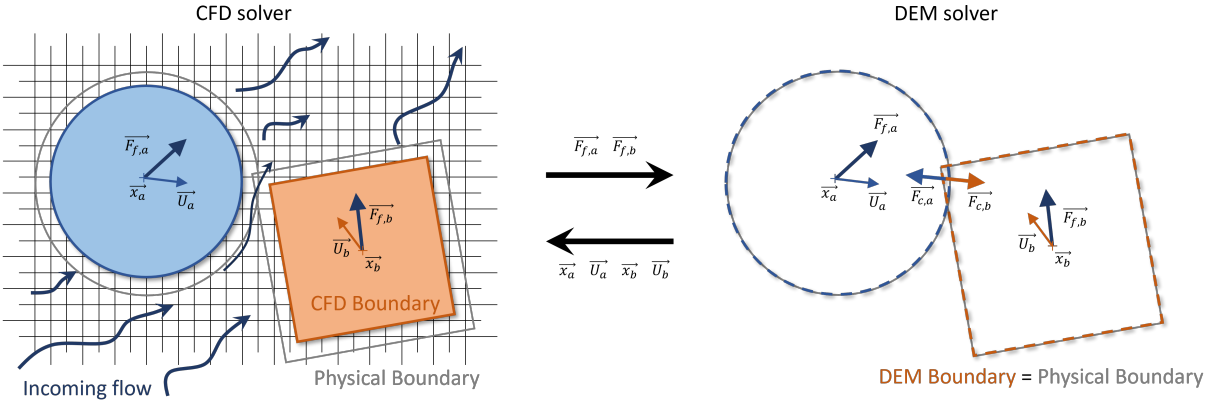

Figure 4: Data exchange between the CFD and DEM solvers during a contact between two particles (a) and (b). The DEM boundary is the same as the physical boundary, but the radius of the discrete forcing boundary is slightly reduced to leave space and enable a proper reconstruction of the walls.

In order to model the contacts inside the fluid solver, the DEM and CFD codes have to be coupled. In this case, the CFD solver acts as the leading code and the DEM solver as an external library. Their interaction is summarized in Figure 4, and a sequence diagram of their interaction is presented in Figure 5 with referenced step in parenthesis. When the fluid solver calls the fluid-structure interaction module, it starts by computing the fluid forces (1) that act on each object (which are defined using the cut-cell method presented in section 2.2.3). A centered temporal scheme is used: the fluid force is first calculated at time step n, then a relaxation of 0.5 is applied with the previous time step before being transferred to the DEM solver. Then, the force on each object is sent to the DEM code which performs the calculations of the contact forces between every object (2). Once all the forces are determined (i.e. fluid, contact and gravity forces), they are summed to obtain the total forces applied on every object:

$$\vec{F}_{tot} = \vec{F}_{f,centered} + \vec{F}_c + \vec{F}_g \tag{21}$$

The DEM code then determines the displacement of the objects over a period of a DEM time step Δt_{DEM} (3). As the DEM time step is, by nature, one or several orders of magnitude smaller than the fluid time step Δt_{fluid}, multiple

iterations of the DEM calculation are performed until the physical time spent in the DEM solver is equal to Δt_{fluid}. As a consequence, the fluid forces are not updated during the DEM forces calculations, and the assumption is made that these forces are constant during this period of time. This approximation is realistic for quasi-static and slowly moving objects like in coastal engineering applications. Once the DEM calculation is done, particle positions and velocities are transmitted to the CFD solver. The objects are then updated using the cut-cell method (4) and the fluid flow is solved for the current time step (5). A validation of the coupling can be found in Appendix A.

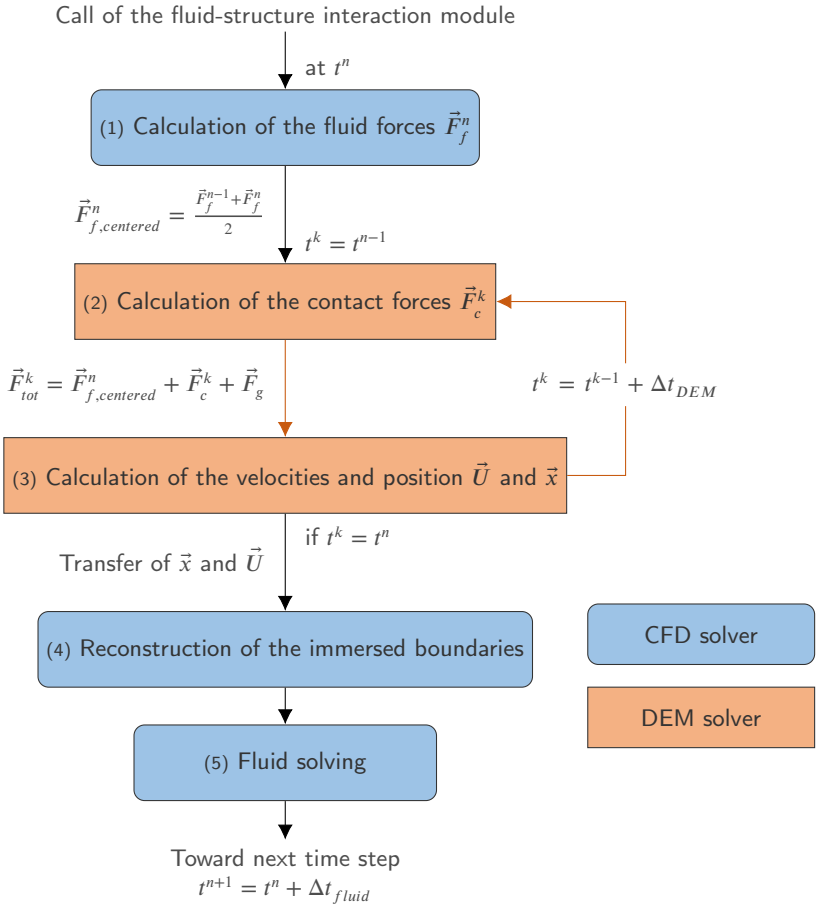

Figure 5: Schematic of the fluid and DEM solvers interactions. n indicates the current CFD time step and k indicates the current DEM time step.

As can be seen in Figure 4, a gap between the particles in the fluid solver is needed in order to perform the discrete forcing reconstruction of the objects. Indeed, having two objects sharing the same cell would require a specific treatment that is not yet available in the fluid solver. To solve this issue and enable a flow between the objects, the discrete forcing boundary has to be artificially reduced or the size of the DEM object has to be increased to leave a gap at least one cell wide. Both options have drawbacks: when the size of the discrete forcing boundary is altered, the interactions between the fluid and the structure are approximated, and the hydrodynamic forces are under evaluated. This can be mitigated by multiplying the forces by the ratio between the real and modeled surfaces. On the other hand, increasing the size of the DEM object can lead to inaccuracies when multiple objects are stacked such as in a two-layer breakwater. For cases with only few interactions between blocks as in section 4, the latter option is chosen as it does not require approximating the fluid-structure interactions driving the calculations. Moreover, the gap between the objects being enlarged, the fluid will have different behaviour (reduction of the Venturi effect where objects are closest can be one of these). The main leverage to mitigate these effects is by building a mesh as refined as possible to reduce the gap between DEM and discrete forcing boundaries.

The coupling system presented in Figure 5 is similar to what has been done between DualSPHysics and Project Chronos (Martínez-Estévez et al., 2023) and the two methods contrast essentially in the type of fluid solver used: a Eulerian-Eulerian CFD solver in this study as opposed to a SPH solver for Martínez-Estévez et al. (2023) and Mitsui et al. (2023). One advantage of using a Eulerian-Eulerian code lies in its capacity to model highly turbulent flows, aerated flows and air entrainment (Mérigoux, 2022). Moreover, the CFD solver neptune_cfd is massively parallel (Mérigoux (2022), Neau et al. (2024)), which gives the possibility to work toward industrial scale cases. On the other hand, SPH methods, being meshless, simplify the representation of closed objects compared to discrete forcing methods. Depending on the aimed purpose, more accurate methods can be employed. For instance, the coupling between OpenFOAM and LIGGGHTS uses feedback forces sent from the DEM solver to the CFD solver and synchronizes the CFD and DEM time steps to ensure optimal convergence of the fluid and particle fields (Razak et al., 2025). However, it requires a very small fluid time step, which can be computationally expensive.

3. Wave forces on a idealised breakwater

The goal of this section is to assess the capacity of the CFD code to predict the forces exerted by breaking waves on an idealised breakwater. Consequently, there is no DEM coupling for this first test case. In-house experiments and simulations are performed, which consist in generating regular waves in a flume toward a set of fixed spheres positioned on a slope representing a schematic breakwater.

3.1. Experimental setup

The experiments took place in a 45 m long, 0.60 m wide and 0.83 m deep wave flume at EDF R&D LNHE in Chatou (France). The general setup of the flume is represented in Figure 6 and pictures of the experimental setup are presented in Figure 7. The still water depth is 0.60 m. During the experiment, regular waves were propagated towards a 2/3 plane slope with fixed spheres mounted on it. The foreshore slope is 4 m long when projected on the x_0 axis, with a 6% slope, which leads the waves to break when reaching the breakwater. The toe of the breakwater is therefore 0.24 m above the bottom of the flume. The 2/3 breakwater slope is 1.5 m long along the x_1 axis.

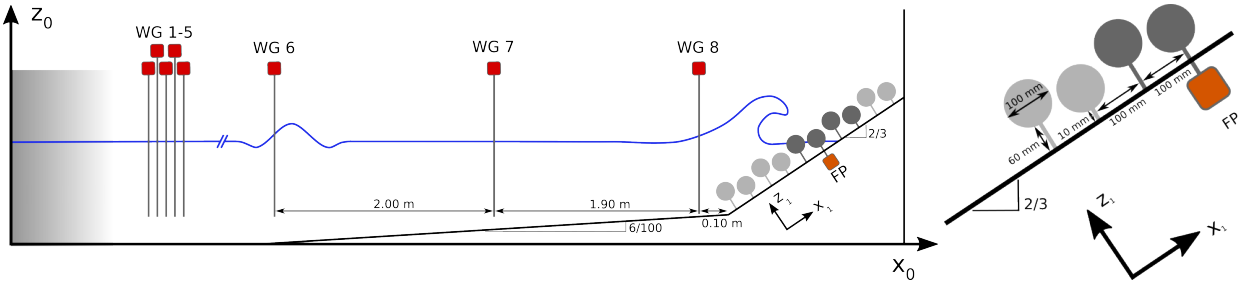

Figure 6: Left: Schematic of the wave flume with wave gauges (WG) and the force probe (FP). Right: Zoom on the breakwater part and the force probe (FP).

The breakwater is composed of a total of thirty-five spheres: thirty-one polystyrene spheres are used to model an idealised breakwater with strong interactions between the waves and the obstacles, and four hollow steel spheres are used to measure the fluid forces acting on them. The polystyrene spheres are coated with polymerized resin in order to ensure their waterproofness. All the spheres have a 100 mm diameter and are placed on a 10 mm diameter steel stem. The polystyrene spheres are embedded and glued over the stem, whereas the steel spheres are welded to the stems. The stems are then screwed onto the breakwater slope. The spheres are positioned on two planes parallel to the breakwater slope in a staggered arrangement. There is a total of ten rows located 100 mm away from each other and starting 50 mm from the breakwater toe (see Figure 6). High (low) spheres are located 100 mm (60 mm) from the slope plane and are 150 mm away from each other (from center to center) in each row.

In order to measure waves, eight wave gauges (WG) of capacitance type with a sampling frequency of 50 Hz are set up during the experiment. This system does not detect air gaps from breaking waves and has limitations when there is air entrainment and aerated flows, which is not the case here (see Figure 10, where the WG is located upstream of the aerated flow). The first five WG are located in front of the wave-maker (the distance from the wave-maker goes from 10.60 m for the closest WG to 11.85 m for the furthest WG), they are far from the slopes and are not perturbed by

Table 1: Location of the wave gauges.

Wave gauge number	WG6	WG7	WG8
x distance from the beginning of the slope (m)	0.0	2.0	3.9

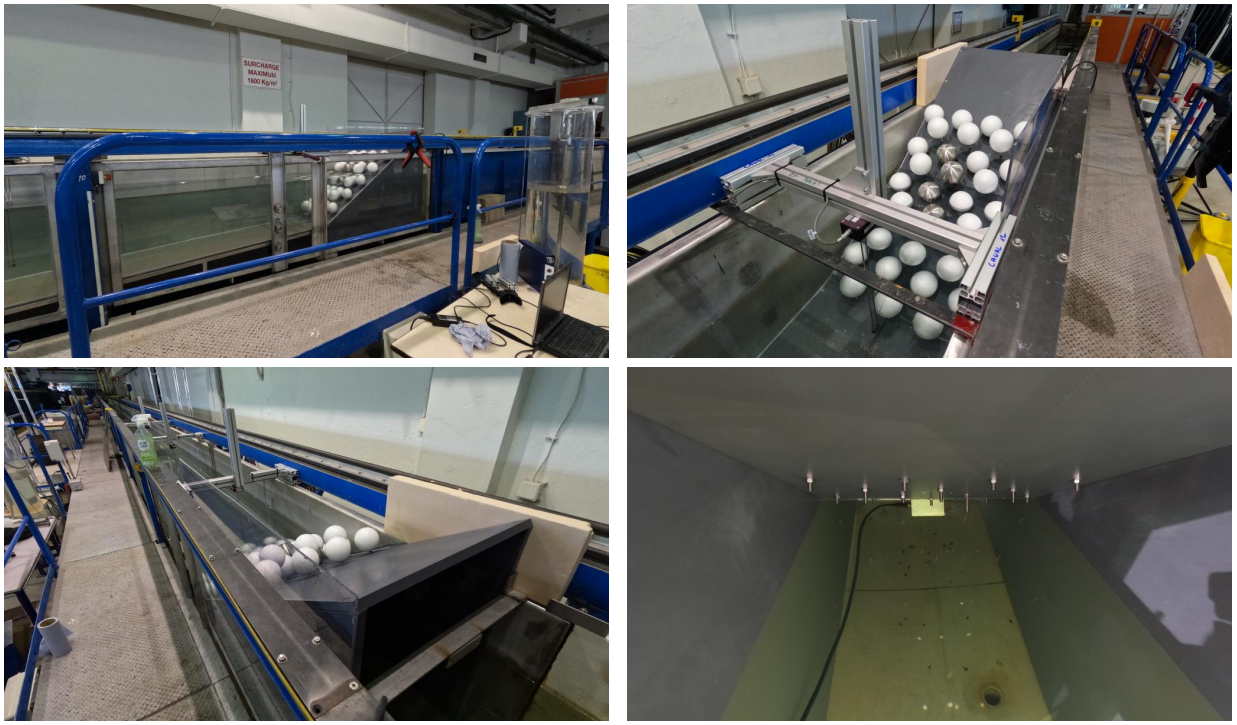

Figure 7: Pictures of the experimental setup. Top-left: global view of the flume and the breakwater. Top-right: Close-up view of the breakwater with a wave gauge in front of the breakwater toe. Bottom-left: global view of the flume seen from behind the idealised breakwater. Bottom-right: View of the back of the breakwater slope with the force probe positioned at its lowest location.

them until the waves reflections reach them on their way back. The furthest one is the one that is used later on, labeled as "WG at inlet". WG6, WG7 and WG8 are located over the 6% foreshore slope: WG6 is just above the beginning of the slope, WG7 at the center of the slope and WG8 0.10 m in front of the breakwater's toe (see locations in table 1).

Four spheres are instrumented with a force probe (FP) in order to measure the time series of forces exerted by the fluid (see the grey spheres in Figure 7 upper-right). The FP is a MC3SSUDW AMTI force probe with a sampling frequency of 2000 Hz to ensure that the force peaks are not overlooked. The rows with instrumented spheres are represented in dark grey in Figure 6. In order to instrument a sphere, its stem goes through the slope and is mounted on the FP which is attached to the slope and does not move (a simple beam computation with a reference fluid force of 10 N applied to the stem gives a deflection of less than 1×10^{-4} m, which is negligible compared to the dimensions of the stems and spheres). In order to seal the hole of the slope through which the stem goes, a small rubber cylinder is positioned at the base of the stem which does not provide any mechanical resistance and ensures that negligible amount of water goes trough the slope. In order to measure the forces on the four spheres each wave condition is repeated four times, with the FP being switched from one sphere to another.

Experimentally, the wave generation is done using a piston-type wave-maker located at the extremity of the flume. Depending on the water depth, it can generate regular waves with periods ranging from 0.5 s to 4 s or irregular waves. The waves are generated using a displacement signal of reference, based on the chosen period and a wave height of 25 cm. The paddle motion is then deduced by multiplying the signal with a span factor. The real wave height is then measured to determine the numerical wave signal, giving the wave parameters presented in table 2. Four wave cases are presented here, labelled from W1 to W4.

Table 2: Wave parameters

Id	Wave period (s)	Wave height (m)	Wavelength (m)
W1	1.3	0.120	2.441
W2	1.3	0.175	2.472
W3	2.0	0.120	4.395
W4	2.0	0.175	4.432

3.2. Numerical setup

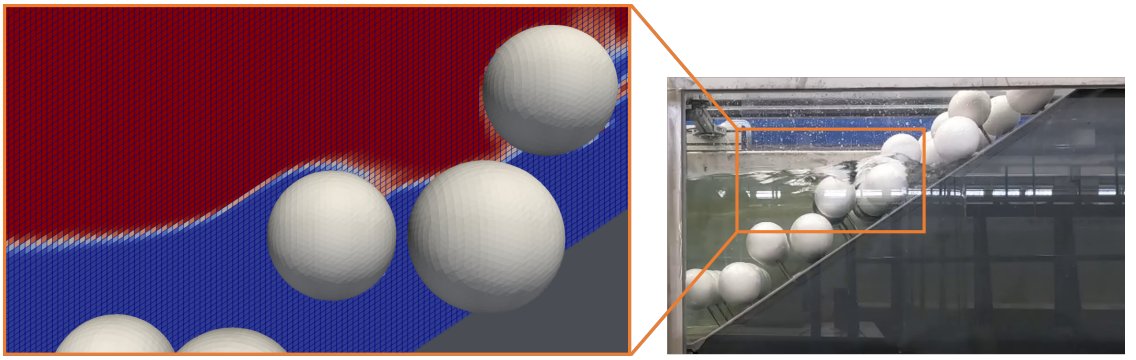

Figure 8: Visualisation of the mesh during a wave impact seen from the side of the flume. Air/water ratio is displayed in red/blue. Mesh size is 20 cells per sphere diameter.

The numerical wave generation is done using the code STREAM_HT (Benoit et al., 2003) which defines a high-order Stokes-type wave based on the so-called stream function approach (Fenton, 1988). It needs the wave period T, the wave height H and the water depth d as input parameters, and determines the free surface elevation and the x and z water velocities. The free surface elevation and the incoming and outgoing velocities are imposed at the inlet of the numerical wave tank. Over one wavelength following the inlet, a relaxation zone is used based on a momentum source term (which is exponentially decreased along x) and represented in grey in the left part of Figure 6. The free surface is defined using the LIM (Large Interface Model). The stems are not represented in the simulations.

The mesh built here is a hexahedral mesh. In the wave propagation zone, the cells are rectangular cuboids with fine refinement near the free surface and coarser refinement at the bottom of the flume and near the top boundary, which is set with a pressure condition (atmospheric conditions). Other boundaries are set as walls using wall law conditions. Over the slopes, the cells are shaped as right rhombic prisms, with a constant cell shape and cell size on the sphere areas. A close up view of the mesh is shown in Figure 8. A mesh sensitivity analysis has been performed and showed that a minimum grid size of 5 mm, which is equivalent to 20 cells per sphere diameter, is necessary to reach converged results (see Appendix C). This leads to a total of 6.6×10^6 cells in the fluid domain. A constant time step of $\Delta t_{fluid} = 1 \times 10^{-3}$ s is used and chosen in order to keep the Courant number below unity.

3.3. Results

The propagation and deformation of the waves for the four wave cases can be observed in Figure 9. The comparison between experiments and simulations shows that the waves are correctly represented. For each wave case, the four repetitions of the experiments are presented and confirm the repeatability of the tests.

Figure 10 shows a side-by-side comparison of experiment and simulation, using for the latter an isosurface at 50% of water. Three camera angles are used: a view from above the flume, a view from inside the flume (in front of the spheres), and a view from the side of the flume, behind a Plexiglas panel. This representation is only shown for the case W4, with five snapshots separated by 0.4 s. At $t = 0.2$ s, the water is fully withdrawn, and the four instrumented spheres are above water. Then, at $t = 0.6$ s, the wave impact occurs, the maximal forces are reached near that instant. At $t = 1.0$ s, the wave reaches its highest point, all instrumented spheres are submerged and forces reach a local minimum or a plateau. At $t = 1.4$ s, the wave is receding, instrumented spheres are partially underwater and forces are still exerted on them. Finally, at $t = 1.8$ s, the water is withdrawn again, but numerous pockets of water and aerated flow remain

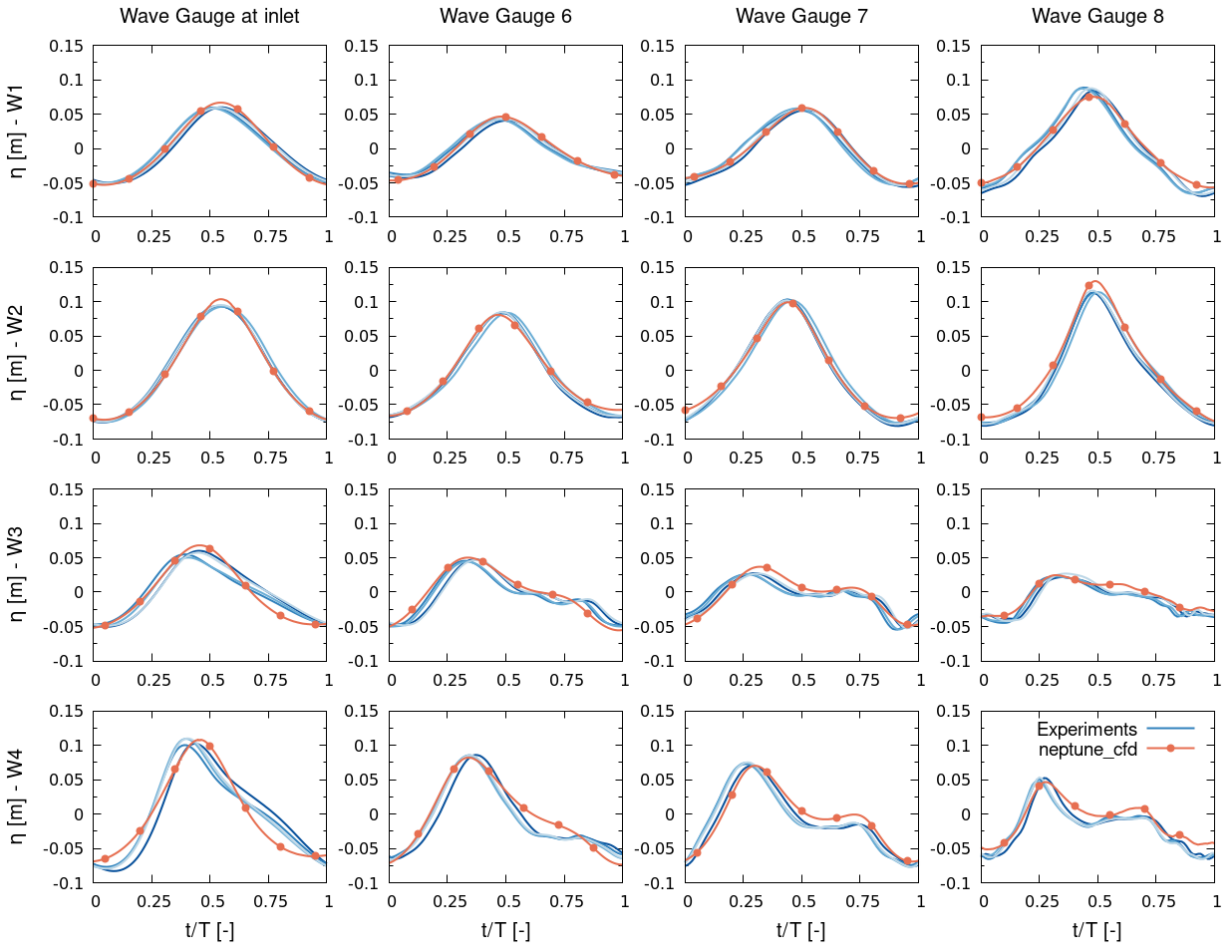

Figure 9: Phase averaged comparison between the experimental and numerical surface elevations (η) at four different locations (the positions of wave gauges from 6 to 8 are indicated in Figure 6, the numerical wave gauge at inlet is located at the numerical boundary of the domain and is therefore not placed at the same location as in the experimental setup). Each wave case is repeated four times in order to place the unique force probe on the four metal spheres, the four wave cases are represented with four shades of blue. The simulation is done only once as the forces can be measured in parallel. The parameters of the waves W1, W2, W3 and W4 can be found in table 2.

close to the spheres. Only one wave is presented here, but the prolongation of the simulation or the experiment does not reveal different behaviours until the waves are affected by the reflection of the first waves.

For the four wave cases, the total force on the four instrumented spheres is presented in Figure 11. Given that the phase-averaged experimental results show vibrations, a filter is applied to take the median value among the 100 nearest time steps (note that the time step of the force probe is 0.5 ms, and the time step of the simulation is 1 ms). The exact origin of these vibrations is not known but might be noise linked to the vibrations of the flume and the slope following the breaking of the wave. The simulation results are close to the experimental results, although generally slightly higher. The plateaus corresponding to 0 N represent the times when the spheres are above water, and therefore when fluid forces are negligible. It can be noted that for cases W1 and W2 (with a period of $T = 1.3$ s and a relatively short wavelength), the waves mainly impact the two bottom spheres. In contrast, for cases W3 and W4 (with a period of $T = 2.0$ s and a longer wavelength), the force magnitude on all four spheres is comparable, although the forces last longer on the two bottom spheres. When comparing the forces on the semi-high sphere and the highest sphere in the W1 and W2 cases, it can be seen that the semi-high sphere is protected from the wave due to its high position relative to the slope, whereas the highest sphere (higher in altitude but closer to the slope) still registers hydrodynamic forces.

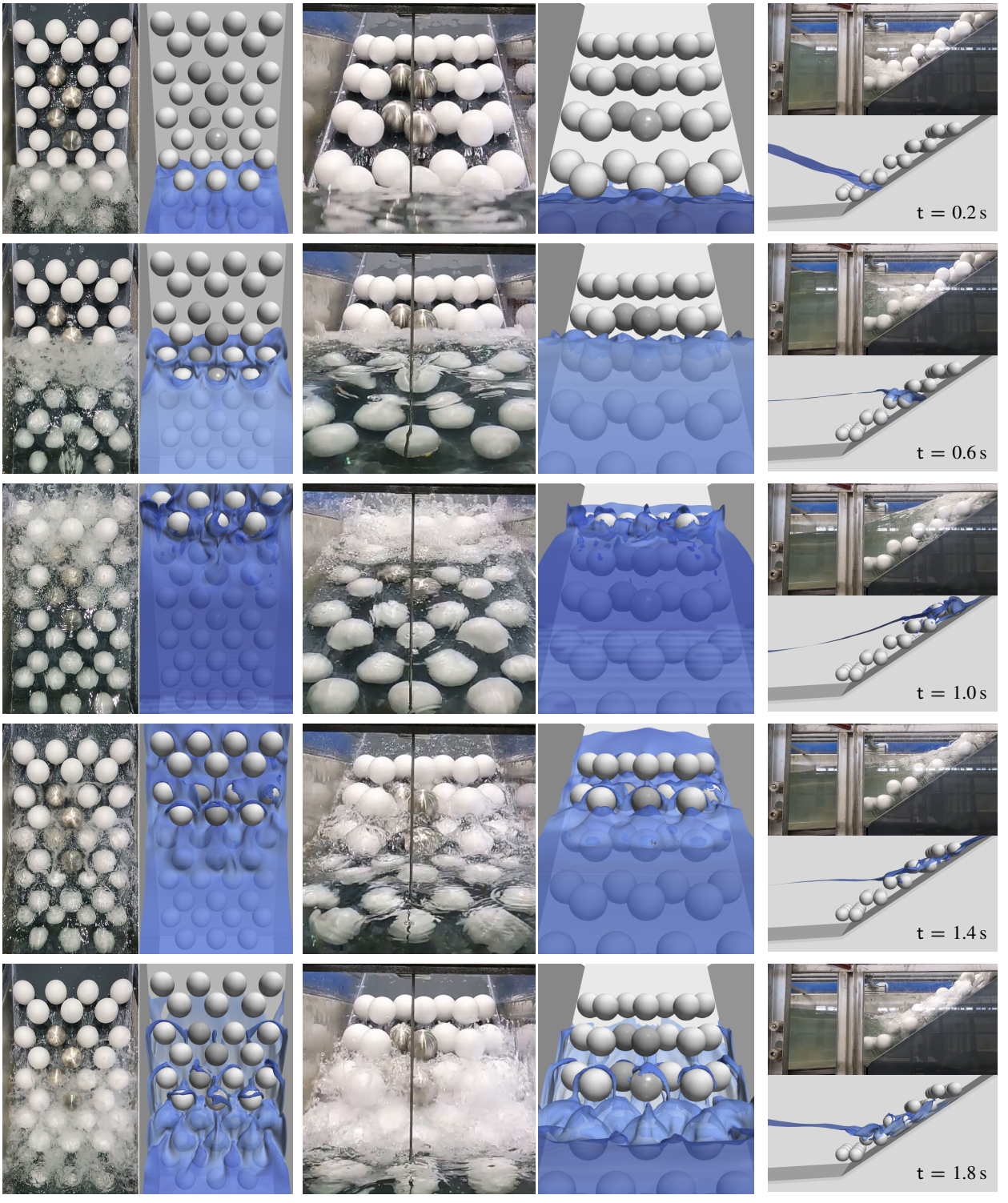

Figure 10: Visual comparison between experiment and simulation for the W4 wave case ($T = 2.0\,s$ and $H = 0.175\,m$). Videos of the experiments are taken using three Gopro cameras placed above, in front of and on the side of the experimental setup, respectively. Simulations visualisations of the free surface are made using an isosurface at 50% of water. Snapshots are presented every $0.4\,s$, one row corresponding to one time instant. The vertical rod in front of the experimental breakwater is the WG8.

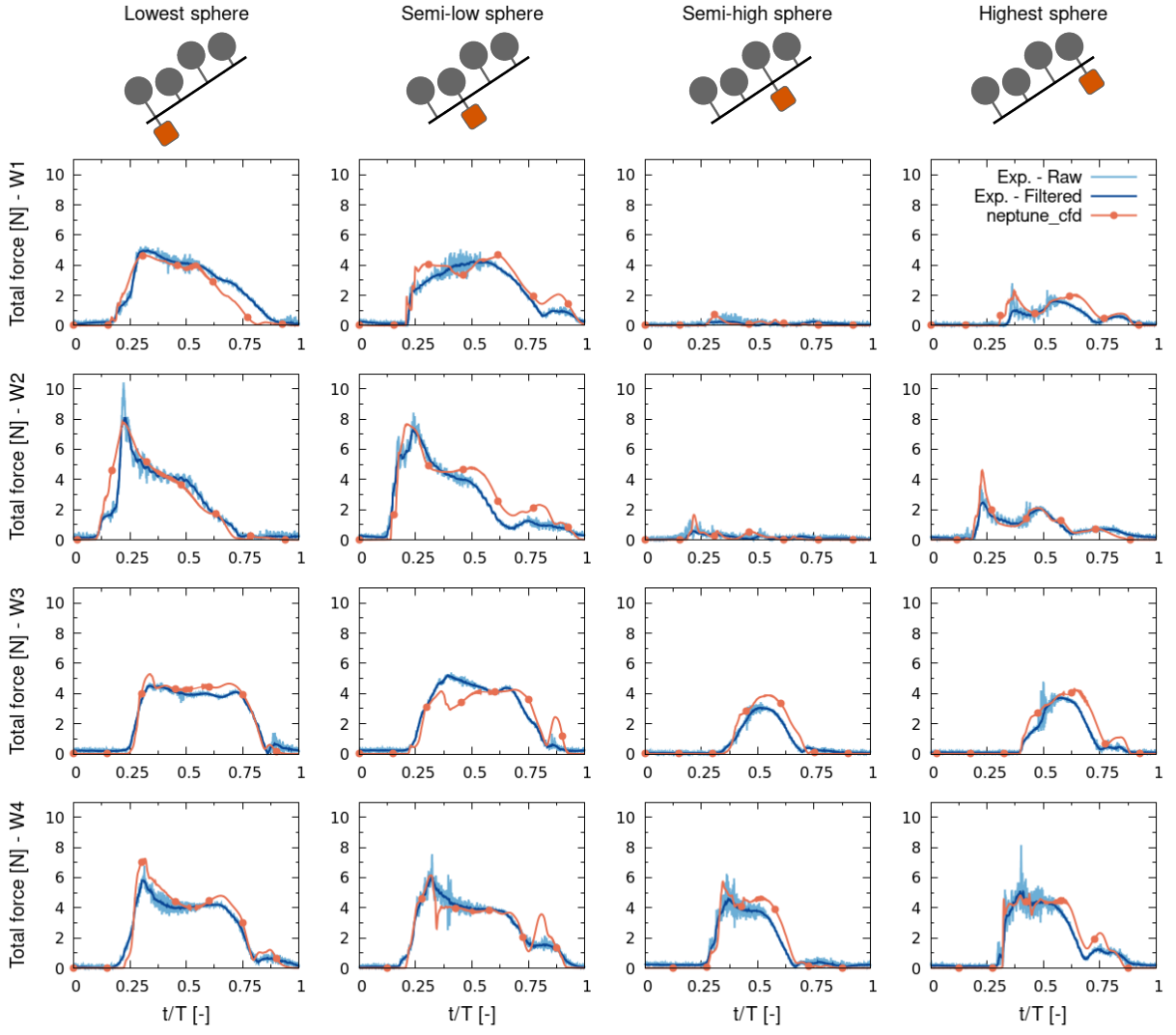

Figure 11: Total phase averaged fluid forces applied on the spheres for four different wave cases. The parameters of the waves W1, W2, W3 and W4 can be found in table 2. Experimental signals are presented raw and filtered, numerical solutions are presented raw (all cases being phase averaged).

4. Impact of a solitary wave on a row of tetrapods

The goal of this section is to show the ability of the present DEM-CFD coupling to reproduce the experiments of Mitsui et al. (2023) which consist in studying the effect of a solitary wave on a row of 15 tetrapods. It is done at a scale of 1:50 compared to prototype scale, with tetrapods of 7.7 cm height. Numerical simulations were also performed in Mitsui et al. (2023), using DualSPHysics to solve the fluid and fluid-structure interactions, and Project Chrono to solve the tetrapod-mound interactions.

4.1. Numerical setup

The experiments reported in Mitsui et al. (2023) were done at Fudo Tetra Corporation in Japan (Matsumoto et al. (2012), Matsumoto et al. (2013)) in a wave flume of 55 m in length, 1.2 m in width and 1.5 m in height, with a water depth of 0.8 m. A mortar slope of 1:30 was made with a small flat PVC mound where the row of tetrapods was placed (note that the tetrapods were made of mortar). The geometric parameters are represented in Figure 12, with the location of the wave gauges (WG) presented in table 3.

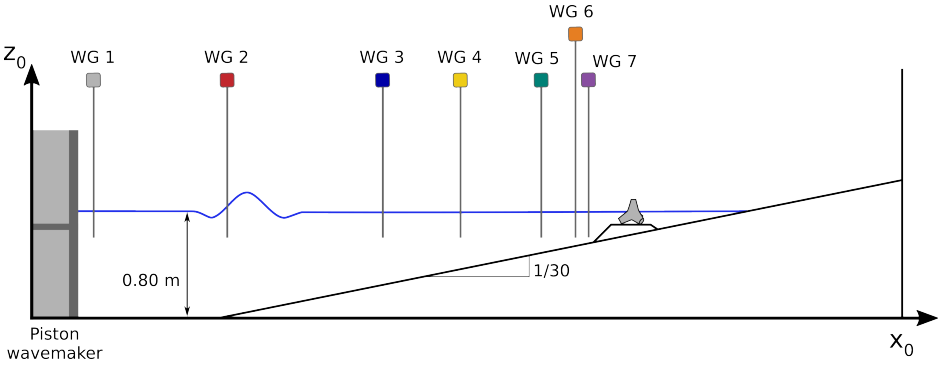

Figure 12: Schematic of the numerical wave flume (not at scale). The coloured squares represent the location of the wave gauges (see coloured curves in Figure 13).

The numerical wave flume uses the same dimensions except for the generation part, as the domain starts at the location of the first wave gauge ($x = 13$ m). The mesh uses hexahedral cells similar to the one presented in section 3. The top boundary is set with a pressure condition (atmospheric conditions) while other boundaries are set as walls using wall law conditions. The characteristic mesh size corresponds to 32 cells per tetrapod height (see Appendix B), resulting in 12.6×10^6 cells in the fluid domain. A constant fluid time step $\Delta t_{fluid} = 5 \times 10^{-4}$ s is used and chosen in order to keep the Courant number below unity, and the DEM time step is chosen as $\Delta t_{DEM} = 1 \times 10^{-5}$ s so that $\Delta t_{fluid}/\Delta t_{DEM} = 50$. The tetrapods are defined as mobile rigid bodies using the Time and Space Dependent Porosity approach with cut-cell functions. The flume, slope, mound and the tetrapods are also represented in the DEM code to model the contacts between rigid bodies. Friction coefficients are taken from Mitsui et al. (2023), with two different values: one for mortar-mortar interactions μ_1 (i.e. between tetrapods and other tetrapods, and between tetrapods and the 1:30 slope) and one for mortar-PVC interactions μ_2 (i.e. between tetrapods and the PVC mound). The mortar-PVC friction coefficient is determined in the original study from a small experiment consisting in pulling a tetrapod over a PVC container filled with water, which gave a mean value of $\mu_2 = 0.32$ with significant dispersion in the measured values. Mitsui et al. (2023) set the mortar/mortar coefficient to $\mu_1 = 0.65$, so we use this value in the following. These authors did not report the coefficient of restitution, hence we use here a value of 0.2 (a sensitivity analysis has shown no influence of this parameter on the results, as the normal impacting velocity is low and the water damps the potential bounces). Additionally, a description of the tetrapod used here to perform the simulations is given in Appendix B.

4.2. Wave generation and propagation

In the experiment, the wave generation is done by a piston-type wave-maker. In order to simulate a wave as close as possible to the real wave, a wave paddle is created at the origin of the flume using the discrete forcing method previously presented. The signal of the paddle is reconstructed using a set of equations presented by Guizien and Barthélemy (2002) based on the Boussinesq solitary wave (Boussinesq (1871), Goring (1978)). The wave then propagates along the flume as shown in Figure 13 where seven WG show the free surface level at different locations along the flume.

Table 3: Location of the wave gauges (WG), the center of the structure being located at $x = 39\,\mathrm{m}$.

Wave gauge number	1	2	3	4	5	6	7
x distance from experimental paddle (m)	13.0	19.0	29.0	33.0	37.0	38.0	38.5

Using this method, three solitary waves are generated (with respective deep water heights of 2.6 cm, 4.5 cm and 6.4 cm) with their height and shape along the flume well reproduced compared to the experiments.

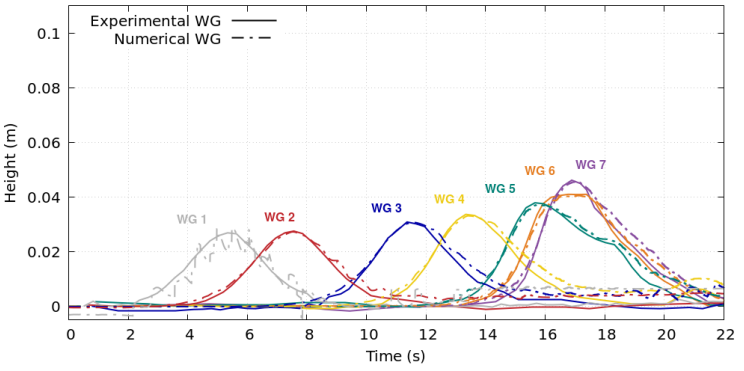

(a) Wave gauges for $H = 2.6\,\mathrm{cm}$

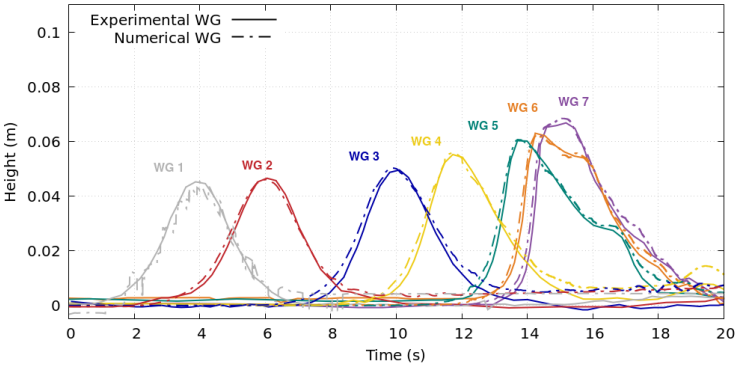

(b) Wave gauges for $H = 4.5\,\mathrm{cm}$

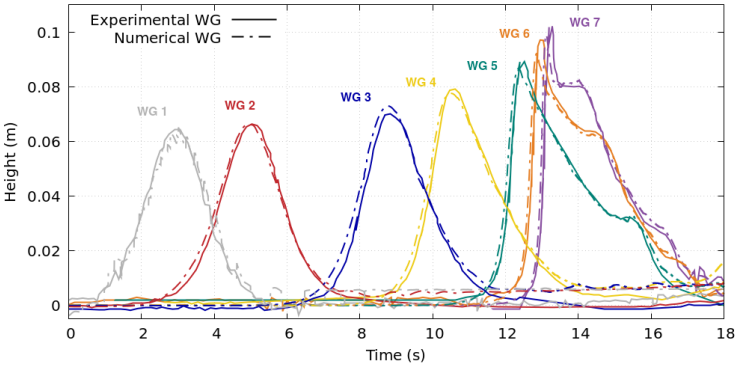

(c) Wave gauges for $H = 6.4\,\mathrm{cm}$

Figure 13: Experimental and numerical wave heights at seven wave gauges (location of the wave gauges Figure 12).

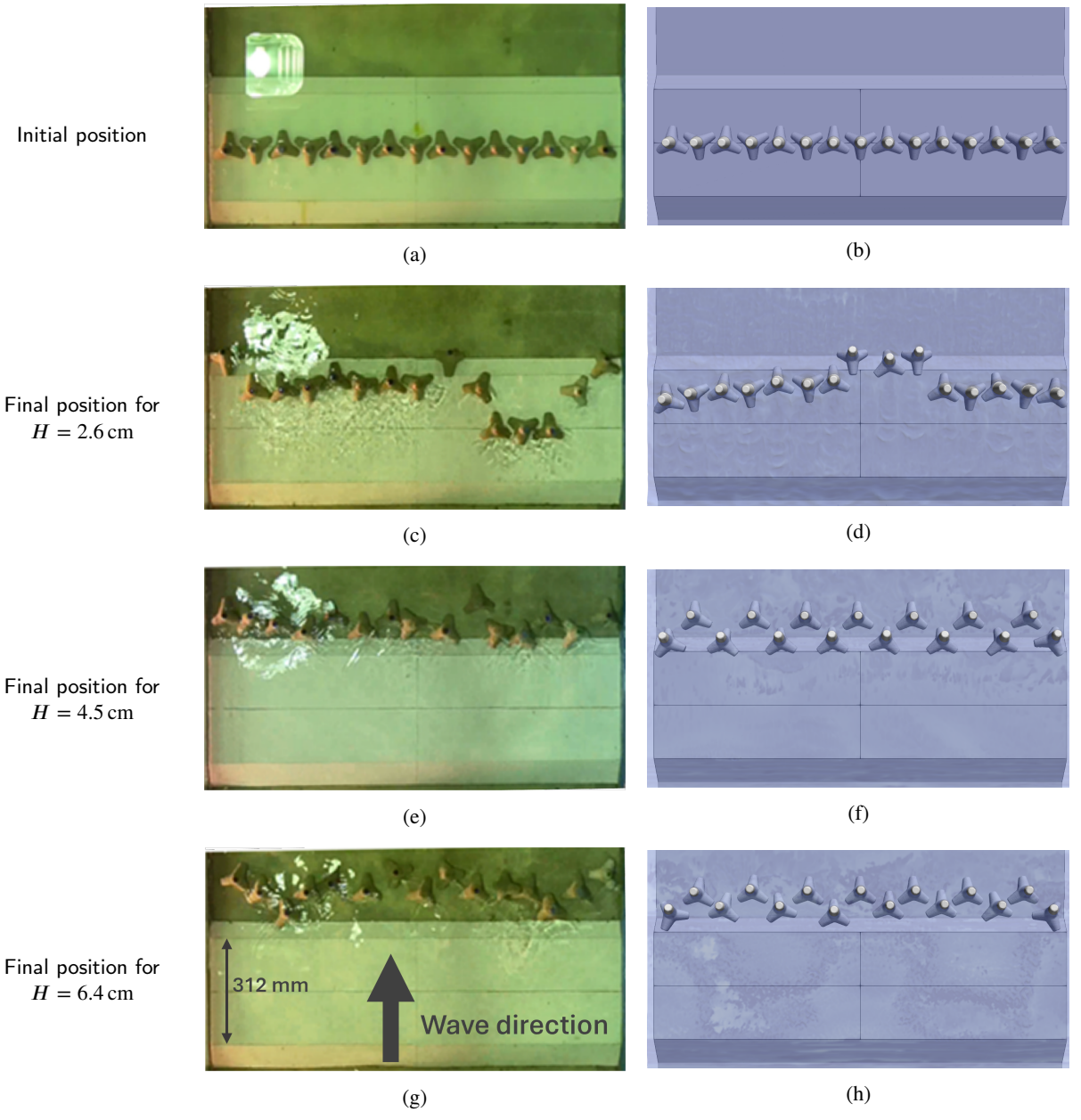

Figure 14: Final position of the tetrapods: (a, c, e, g) Mitsui et al. (2023)'s experiment, (b, d, f, h) present simulations.

4.3. Results

As a result of the wave action, the tetrapods slide on the PVC horizontal mound. After 156 mm of sliding, they fall on the mortar slope and continue to move. A visualisation of the final position of the tetrapods in the experiments and in the simulations is shown in Figure 14. In Figure 15, the final displacement of the tetrapods is shown, each red circle representing one numerical tetrapod and each blue square representing the median of the tetrapods displacements among the three identical experiments conducted, with their minimal and maximal values also represented. Furthermore, the orange triangles represent the results of a similar simulation performed with the addition of a small randomization of the initial placement of the tetrapods, with a rotation of up to ± 2 deg along the z axis and a translation of up to ± 2 mm along the x and y axes. The minimal, average and maximal displacements of the 15 tetrapods are also shown in Figure 16, along with an additional sensitivity analysis of the friction coefficient.

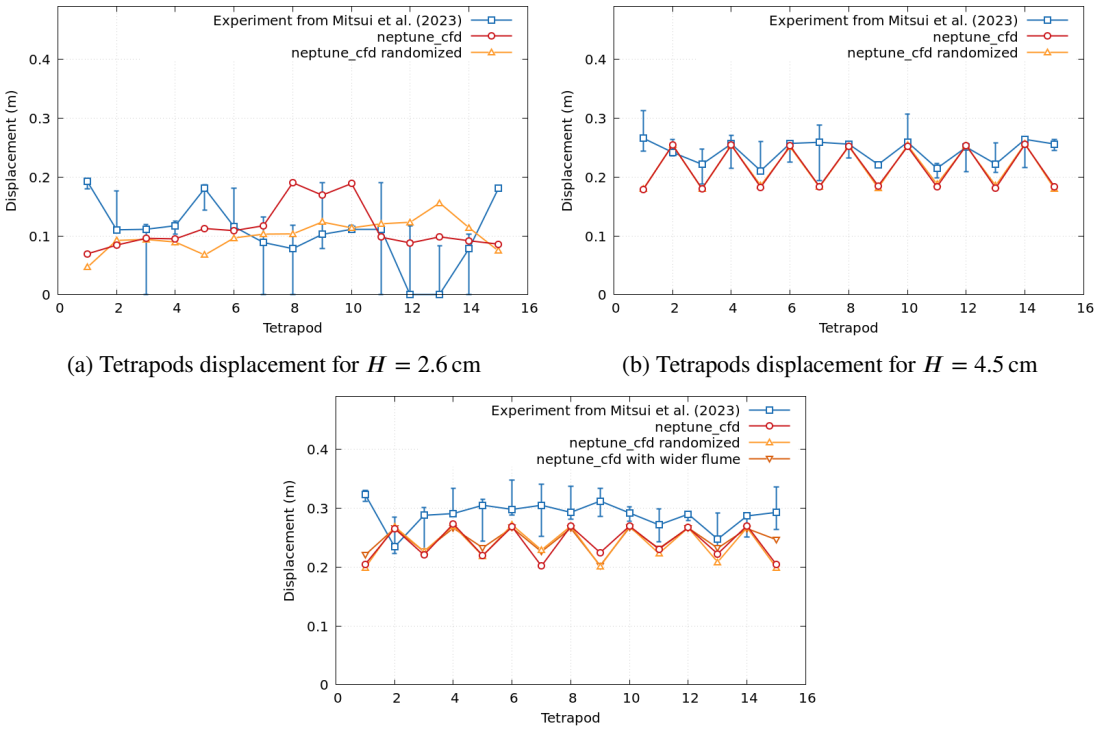

(a) Tetrapods displacement for $H = 2.6\,\text{cm}$

(b) Tetrapods displacement for $H = 4.5\,\text{cm}$

(c) Tetrapods displacement for $H = 6.4\,\text{cm}$

Figure 15: Final displacement of the tetrapods: in blue the minimum, median and maximum values of the three experimental measurements, in red the numerical simulations and in orange the same numerical simulation with a slight randomization of the initial position of the tetrapods (up to $\pm 2\,\text{deg}$ along the z axis and up to $\pm 2\,\text{mm}$ along the x and y axis). Each abscissa corresponds to a tetrapod.

For the first case with a wave height $H = 2.6\,\text{cm}$, experimental results show significant dispersion ranging from no displacement at all to almost 20 cm, corresponding to some tetrapods falling from the mound (see Figure 14c). Numerical results show less variability in the displacement, even though 3 tetrapods also reach the end of the mound as opposed to most of the tetrapods that stay on the mound. The randomized simulation confirms that the displacement is highly dependent on the initial placement and orientation of the tetrapods which is coherent with the large differences obtained between the three experimental repetitions. In addition, the side walls seem to increase the final displacement of the tetrapods in the experiments while they seem to reduce it in the numerical simulations. This behaviour can be observed in the two other cases, as well as in the SPH simulations performed by Mitsui et al. (2023). For the simulations performed in the current study, it might be explained by the increased DEM size of the tetrapods which can increase the interactions between the tetrapods and the walls compared to the experiments. A tentative simulation performed in a flume extended on both sides by 5 cm for the $H = 6.4\,\text{cm}$ wave case (see Figure 15) shows that the wall proximity indeed impacts the total displacement of the lateral tetrapods. This effect is not found for the central tetrapods as they move as a coherent group. Experimentally, the second and third cases ($H = 4.5\,\text{cm}$ and $H = 6.4\,\text{cm}$) show less variability, even though extreme displacements still occur. As opposed to the $H = 2.6\,\text{cm}$ case, all the tetrapods fall down the step and some of them slide on the mortar slope. For both of these cases, the numerical simulations show results close to the experimental range of displacement although numerical average and maximum values are noticeably lower than their experimental counterparts. The difference in the variability of the displacement can also be found in the variability of the rotation of the tetrapods (see Figure 14g vs 14h for instance). The simulations tend to align the tetrapods in the same direction (half of them already being in the right alignment, half of them tipping over while falling from the step). On the contrary, the experimental study shows a wide range of alignments, especially for the intermediate case $H = 4.5\,\text{cm}$. Furthermore, the results of the randomized simulations for the 4.5 cm and 6.4 cm

wave cases show that these cases are less sensitive to the initial conditions compared to the 2.6 cm wave case. This is coherent with the experimental results, as the tetrapods are less spread with the higher waves than with the lowest one.

The difference between numerical and experimental results may be partly explained by the high variability of the experimental measures due to physical factors which are not numerically represented (such as the variation of the friction coefficient, the mass variability among tetrapods, the degradation of the tetrapods between the beginning and the end of the experiments, the potential lateral asymmetry of the wave, etc.). Other numerical approximations are also made to fill unknown parameters or to facilitate the simulations, such as the shape of the tetrapod which is represented with an assembly of four truncated cones which is slightly different from reality. Another example is the coefficient of normal restitution for a mortar tetrapod impacting a mortar slope when falling from a step, which is unknown and can only be estimated (a value of 0.2 was used here). However, a sensitivity study has shown that this factor does not impact the results in this specific case.

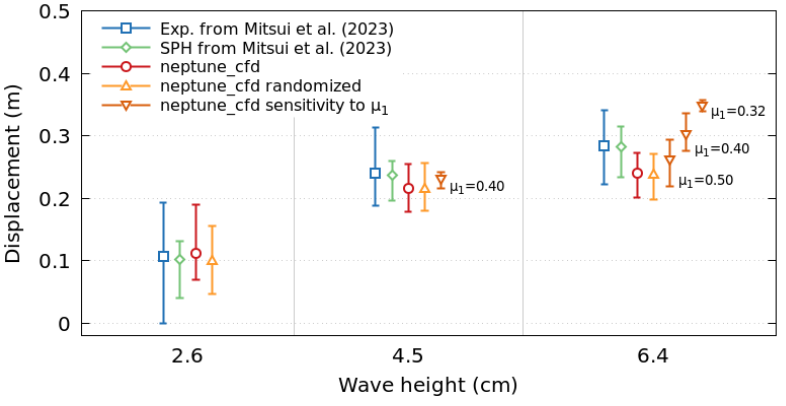

Figure 16: Minimum, average and maximum displacements of the tetrapods. *Randomized* indicates that the initial positions have been randomized (up to ±2 deg along the z axis and up to ±2 mm along the x and y axis). Specified values of μ_1 indicates the value of the friction coefficient between the slope and the tetrapods ($\mu_1 = 0.65$ if not specified).

The impact of the friction coefficient μ_1 between the tetrapods and the slope (mortar/mortar) is presented in Figure 16, along with the experimental results from Mitsui et al. (2023) and their SPH simulations. Indeed, the original study presents an experimental measurement of the tetrapod/mound (mortar/PVC) friction coefficient μ_2 as well as a numerical sensitivity study, but gives less information regarding how μ_1 was obtained. Concerning the sensitivity study of μ_2, similar results compared to those presented by Mitsui et al. (2023) were obtained here (not shown). Focusing on μ_1, various values can be found approximately ranging from 0.4 to 0.8 for dry setups and likely to be lower in wet conditions. In the original study, μ_1 is taken as equal to 0.65 and is not discussed. Here, three other values of μ_1 are tested: 0.50, 0.40 and 0.32. The 0.50 and 0.40 values aim to depict realistic conditions for immersed mortar/mortar interaction which could have happened in the experiment, while the 0.32 value is the tetrapod/PVC friction coefficient chosen for μ_2. As no tetrapod falls off the mound for the 2.6 cm wave case, no result is presented.

For the 4.5 cm wave case, the tetrapods fall at the base of the mound and the higher friction coefficient tends to uniformize the fall by preventing the legs of the tetrapods from blocking the motions when impacting the slope. The most impacted simulation is the 6.4 cm wave case, with a mean displacement increase of about one tetrapod length for the friction coefficient $\mu_1 = 0.40$. If the reference simulation ($\mu_1 = 0.65$) was mainly in the lower bound of the experimental distribution, the simulation with $\mu_1 = 0.40$ reaches the higher bound of the experimental displacements. As this parameter is sensitive to local conditions and to the roughness at the surface of the rigid bodies, a high variability of the real friction coefficient could explain the discrepancies between experimental and numerical results. The results with $\mu_1 = 0.32$ show a different behaviour with unusually low dispersion, which is in line with a reduction of the dispersion when the friction coefficient diminishes.

Overall, the present simulations are in fair agreement with Mitsui et al. (2023)'s experiments and simulations. In addition, we highlight here the significant effect of the local friction coefficient on the displacement of armour blocks, and argue that this parameter should be carefully measured or estimated in order to obtain quantitative predictions.

5. Conclusion

This study introduces a CFD-DEM coupling method for coastal engineering and environmental applications. The CFD code used here effectively simulates free-surface flows and fluid-solid interactions involving complex-shaped moving bodies. It presents several industrial advantages such as its capacity to model highly turbulent or aerated flows and its massively parallel capabilities. Additionally, the DEM code used in this study can efficiently model the contacts between a high number of complex rigid objects. The coupling between both codes aims to address challenges involving contacts between several objects and fluid dynamics at an industrial scale.

A first validation case is presented to demonstrate the ability of the fluid solver to evaluate the forces of waves impacting coastal structures. To do so, an original experimental campaign was performed in a laboratory flume, with fixed idealised spherical armour units instrumented with a force probe. Simulations are performed with a similar configuration and results are compared to the experiment. After that, a wave impact on a row of tetrapods is simulated based on an experimental study, showing the capacity of the numerical model to represent complex fluid-structure interaction effects. Additionally, we highlight the crucial role of solid-solid friction (via the specific value of the friction coefficient of each material) in controlling the displacement of armour blocks for this specific scenario.

The research presented in this study has demonstrated the significant potential of CFD-DEM coupling methods toward the simulations of realistic scenarios of wave interaction with breakwaters. Future works will aim to model and simulate the impact of waves over sections of non-idealized breakwaters, to investigate the underlying mechanisms of breakwater degradation and failure. Realistic breakwaters typically consist of multiple armour layers and a greater number of armour units, closely stacked together. Such simulation would require the optimization of the current method, as well as deeper analysis of the flow between the units. Furthermore, the extension of this work to highly aerated and turbulent flows could be made possible thanks to the development of the Generalized Large Interface Model (GLIM) in the CFD code, which enables the statistical modeling of bubbles at the sub-grid level. The use of this model was considered unnecessary here following a sensitivity analysis, but could play a key role in situations involving sediment transport or multi-scale calculations. Besides, the current studies are based on single sized armour units over an impermeable soil, whereas breakwaters are usually permeable and feature various scales of rockfill materials from rocks to gravel and sand. The multiscale nature of the problem necessitates the integration of multiple approaches to complete the presented modeling of the wave-armour blocks interaction.

Acknowledgements

The authors warmly thank the team of EDF R&D LNHE (Clément Buvat, Nicolas Guéguen, Anthony Jouan) who performed the wave flume experimental study presented in section 3.

The present work has been realized in the framework of the joint team called ICMF2E (Institut Commun de Mécanique des Fluides pour l'Energie et l'Environnement), a collaboration between IMFT and EDF R&D on fluid mechanic applications for energy, environment and processes.

References

Altomare, C., Gironella, X., 2014. An experimental study on scale effects in wave reflection of low-reflective quay walls with internal rubble mound for regular and random waves. Coastal Engineering 90, 51–63. doi:10.1016/j.coastaleng.2014.04.002.

Baird, W.F., Caldwell, J.M., Edge, B.L., Magoon, O.T., Treadwell, D.D., 1980. Report on the damages to the Sines breakwater, Portugal. Coastal Engineering Proceedings 17, 3063–3077. doi:10.9753/icce.v17.181.

Bao, X., Wu, H., Xiong, H., Chen, X., 2023. Particle shape effects on submarine landslides via CFD-DEM. Ocean Engineering 284, 115140. doi:10.1016/j.oceaneng.2023.115140.

Benguigui, W., Doradoux, A., Lavieville, J., Mimouni, S., Longatte, E., 2018. A discrete forcing method dedicated to moving bodies in two-phase flow: Time- and space-dependent porosity method. International Journal for Numerical Methods in Fluids 88, 315–333. doi:10.1002/fld.4670.

Benguigui, W., Laviéville, J., Merigoux, N., 2019. Fluid-structure interaction in two-phase flow using a discrete forcing method. International Journal for Numerical Methods in Fluids 91, 247–261. doi:10.1002/fld.4753.

Benguigui, W., Peyrard, C., 2024. CFD numerical approach based on a discrete forcing method for FOWT, in: 19e Journées de l'Hydrodynamique, Nantes.

Benoit, M., Benguigui, W., Teles, M., Robaux, F., Peyrard, C., 2023. Two-phase CFD Simulation of Breaking Waves Impacting a Coastal Vertical Wall with a Recurved Parapet. International Journal of Offshore and Polar Engineering 33, 123–131. doi:10.17736/ijope.2023.sv03.

Benoit, M., Luck, M., Chevalier, C., Belorgey, M., 2003. Near-bottom kinematics of shoaling and breaking waves: experimental investigation and numerical prediction, in: Coastal Engineering 2002, World Scientific Publishing Company, Cardiff, Wales. pp. 306–318. doi:10.1142/9789812791306_0027.

Bergen, G.V.D., 1999. A Fast and Robust GJK Implementation for Collision Detection of Convex Objects. Journal of Graphics Tools 4, 7–25. doi:10.1080/10867651.1999.10487502.

Bonus, J., Spröer, F., Winter, A., Arduino, P., Krautwald, C., Motley, M., Goseberg, N., 2025. Tsunami debris motion and loads in a scaled port setting: Comparative analysis of three state-of-the-art numerical methods against experiments. Coastal Engineering 197, 104672. doi:10.1016/j.coastaleng.2024.104672.

Bouscasse, B., Colagrossi, A., Marrone, S., Antuono, M., 2013. Nonlinear water wave interaction with floating bodies in SPH. Journal of Fluids and Structures 42, 112–129. doi:10.1016/j.jfluidstructs.2013.05.010.

Boussinesq, J., 1871. Théorie de l'intumescence liquide, appelée onde solitaire ou de translation, se propageant dans un canal rectangulaire. Les Comptes Rendus de l'Académie des Sciences 72, 755–759.

Burcharth, H.F., 1987. The lessons from recent breakwater failures. Developments in breakwater design, in: Technical Congress on Inshore Engineering, Vancouver, Canada.

Chen, J., Wang, L., Yang, S., Zhang, J., 2025. Semi-resolved CFD–DEM coupling simulation of wave interaction with submerged permeable breakwaters. Ocean Engineering 321, 120411. doi:10.1016/j.oceaneng.2025.120411.

Chen, J., Zhang, J., 2023. Semi-resolved CFD-DEM coupling model for submerged granular collapse. Powder Technology 425, 118624. doi:10.1016/j.powtec.2023.118624.

Chen, Q., Zang, J., Dimakopoulos, A.S., Kelly, D.M., Williams, C.J., 2016. A Cartesian cut cell based two-way strong fluid–solid coupling algorithm for 2D floating bodies. Journal of Fluids and Structures 62, 252–271. doi:10.1016/j.jfluidstructs.2016.01.008.

CIRIA, CUR, CETMEF, 2007. The Rock Manual - The use of rock in hydraulic engineering (2nd edition). C683, CIRIA, London.

Coste, P., 2013. A Large Interface Model for two-phase CFD. Nuclear Engineering and Design 255, 38–50. doi:10.1016/j.nucengdes.2012.10.008.

Coste, P., Laviéville, J., 2015. A turbulence model for large interfaces in high Reynolds two-phase CFD. Nuclear Engineering and Design 284, 162–175. doi:10.1016/j.nucengdes.2014.12.004.

Cundall, P.A., 1971. A computer model for simulating progressive, large-scale movement in blocky rock system. Proceedings of the International Symposium on Rock Mechanics .

Ding, D., Ouahsine, A., Xiao, W., Du, P., 2021. CFD/DEM coupled approach for the stability of caisson-type breakwater subjected to violent wave impact. Ocean Engineering 223, 108651. doi:10.1016/j.oceaneng.2021.108651.

Džiugys, A., Peters, B., 2001. An approach to simulate the motion of spherical and non-spherical fuel particles in combustion chambers. Granular Matter 3, 231–266. doi:10.1007/PL00010918.

Fenton, J., 1988. The numerical solution of steady water wave problems. Computers & Geosciences 14, 357–368. doi:10.1016/0098-3004(88)90066-0.

van Gent, M.R., van der Werf, I.M., 2014. Rock toe stability of rubble mound breakwaters. Coastal Engineering 83, 166–176. doi:10.1016/j.coastaleng.2013.10.012.

Gilbert, E., Johnson, D., Keerthi, S., 1988. A fast procedure for computing the distance between complex objects in three-dimensional space. IEEE Journal on Robotics and Automation 4, 193–203. doi:10.1109/56.2083.

Gondret, P., Lance, M., Petit, L., 2002. Bouncing motion of spherical particles in fluids. Physics of Fluids 14, 643–652. doi:10.1063/1.1427920.

Goring, D.G., 1978. Tsunamis – The Propagation of Long Waves onto a Shelf. Ph.D. thesis. California Institute of Technology. Doi: 10.7907/Z9W957BN.

Guelfi, A., Bestion, D., Boucker, M., Boudier, P., Fillion, P., Grandotto, M., Hérard, J.M., Hervieu, E., Péturaud, P., 2007. NEPTUNE: A New Software Platform for Advanced Nuclear Thermal Hydraulics. Nuclear Science and Engineering 156, 281–324. doi:10.13182/NSE05-98.

Guizien, K., Barthélemy, E., 2002. Accuracy of solitary wave generation by a piston wave maker. Journal of Hydraulic Research 40, 321–331. doi:10.1080/00221680209499946.

Han, X., Dong, S., 2023. Interaction between regular waves and floating breakwater with protruding plates: Laboratory experiments and SPH simulations. Ocean Engineering 287, 115906. doi:10.1016/j.oceaneng.2023.115906.

Hudson, R.Y., 1959. Laboratory Investigation of Rubble-Mound Breakwaters. Journal of the Waterways and Harbors Division 85, 93–121. doi:10.1061/JWHEAU.0000142.

Huet, D.P., Jalaal, M., van Beek, R., van der Meer, D., Wachs, A., 2021. Granular avalanches of entangled rigid particles. Physical Review Fluids 6, 104304. doi:10.1103/PhysRevFluids.6.104304.

Iribarren, R., 1938. Una formula para el calculo de los diques de escollera. M. Bermejillo Usabiaga, Pasajes, Guipuzcoa, España .

Ishii, M., 1975. Thermo-Fluid Dynamics of Two-Phase Flow. volume 22 of *Direction des études et recherches d'Electricité de France*. Eyrolles, Paris.

Izard, E., Lacaze, L., Bonometti, T., Pedrono, A., 2018. Numerical Modeling of a Granular Collapse Immersed in a Viscous Fluid, in: Gourbesville, P., Cunge, J., Caignaert, G. (Eds.), Advances in Hydroinformatics. Springer Singapore, Singapore, pp. 1099–1116. doi:10.1007/978-981-10-7218-5_76.

Jensen, O.J., 2024. Safety of Breakwater Armour Layers with Special Focus on Monolayer Armour Units. Marine and Coastal Engineering .

Jiang, M., Shen, Z., Wu, D., 2018. CFD-DEM simulation of submarine landslide triggered by seismic loading in methane hydrate rich zone. Landslides 15, 2227–2241. doi:10.1007/s10346-018-1035-8.

Koo, W., Kim, M.H., 2004. Freely floating-body simulation by a 2D fully nonlinear numerical wave tank. Ocean Engineering 31, 2011–2046. doi:10.1016/j.oceaneng.2004.05.003.

Losada, M.A., Gimenez-Curto, L.A., 1979. The joint effect of the wave height and period on the stability of rubble mound breakwaters using Iribarren's number. Coastal Engineering 3, 77–96. doi:10.1016/0378-3839(79)90011-5.

Ma, H., Zhou, L., Liu, Z., Chen, M., Xia, X., Zhao, Y., 2022. A review of recent development for the CFD-DEM investigations of non-spherical particles. Powder Technology 412, 117972. doi:10.1016/j.powtec.2022.117972.

Martínez-Estévez, I., Domínguez, J., Tagliafierro, B., Canelas, R., García-Feal, O., Crespo, A., Gómez-Gesteira, M., 2023. Coupling of an SPH-based solver with a multiphysics library. Computer Physics Communications 283, 108581. doi:10.1016/j.cpc.2022.108581.

Matsumoto, A., Mano, A., Mistui, J., Hanzawa, M., 2012. Stability prediction on armor blocks for submerged breakwater by Computational Fluid Dynamics. Coastal Engineering Proceedings , 23doi:10.9753/icce.v33.structures.23.

Matsumoto, A., Mano, A., Mitsui, J., Hanzawa, M., 2013. Armor Block Stability of Submerged Breakwaters Predicted by Numerical Wave Flume. Journal of Coastal Research 65, 338–343. doi:10.2112/SI65-058.1.

Mer, S., Praud, O., Neau, H., Merigoux, N., Magnaudet, J., Roig, V., 2018. The emptying of a bottle as a test case for assessing interfacial momentum exchange models for Euler–Euler simulations of multi-scale gas-liquid flows. International Journal of Multiphase Flow 106, 109–124. doi:10.1016/j.ijmultiphaseflow.2018.05.002.

Mitsui, J., Altomare, C., Crespo, A.J., Domínguez, J.M., Martínez-Estévez, I., Suzuki, T., Kubota, S.i., Gómez-Gesteira, M., 2023. DualSPHysics modelling to analyse the response of Tetrapods against solitary wave. Coastal Engineering 183, 104315. doi:10.1016/j.coastaleng.2023.104315.

Mérigoux, N., 2022. Multiphase Eulerian-Eulerian CFD supporting the nuclear safety demonstration. Nuclear Engineering and Design 397, 111914. doi:10.1016/j.nucengdes.2022.111914.

Neau, H., Ansart, R., Baudry, C., Fournier, Y., Mérigoux, N., Koren, C., Laviéville, J., Renon, N., Simonin, O., 2024. HPC challenges and opportunities of industrial-scale reactive fluidized bed simulation using meshes of several billion cells on the route of Exascale. Powder Technology 444, 120018. doi:10.1016/j.powtec.2024.120018.

Rakotonirina, A.D., 2018. Grains3D, a flexible DEM approach for particles of arbitrary convex shape - Part II: Parallel implementation and scalable performance. Powder Technology , 18.

Rakotonirina, A.D., Delenne, J.Y., Radjai, F., Wachs, A., 2019. Grains3D, a flexible DEM approach for particles of arbitrary convex shape—Part III: extension to non-convex particles modelled as glued convex particles. Computational Particle Mechanics 6, 55–84. doi:10.1007/s40571-018-0198-3.

Razak, R., Alosail, M.S., Musa, K.I., Gago, P.A., Hussain, S., Chen, Z., Tyson, S., Rahman, S.S., 2025. Spatially resolved CFD-DEM model with innovative experimental validation methods to improve understanding of sand retention in oil and gas wells with the consideration of filter-beds on standalone screens. Powder Technology 449, 120406. doi:10.1016/j.powtec.2024.120406.

Rongé, E., Peyrard, C., Venugopal, V., Xiao, Q., Johanning, L., Benoit, M., 2023. Evaluation of second and third-order numerical wave-loading models for floating offshore wind TLPs. Ocean Engineering 288, 116064. doi:10.1016/j.oceaneng.2023.116064.

Salis, N., Hu, X., Luo, M., Reali, A., Manenti, S., 2024. 3D SPH analysis of focused waves interacting with a floating structure. Applied Ocean Research 144, 103885. doi:10.1016/j.apor.2024.103885.

Sarfaraz, M., Pak, A., 2018. Numerical investigation of the stability of armour units in low-crested breakwaters using combined SPH–Polyhedral DEM method. Journal of Fluids and Structures 81, 14–35. doi:10.1016/j.jfluidstructs.2018.04.016.

Scaravaglione, G., Latham, J.P., Xiang, J., Francone, A., Tomasicchio, G.R., 2022. Historical overview of the structural integrity of Concrete Armour Units. Coastal and Offshore Science and Engineering , 68–98.

Scaravaglione, G., Marino, S., Francone, A., Leone, E., Damiani, L., Tomasicchio, G.R., Van Gent, M.R., Saponieri, A., 2025. The influence of shallow water on rock armour stability. Coastal Engineering 197, 104657. doi:10.1016/j.coastaleng.2024.104657.

Senturk, B.U., Guler, H.G., Baykal, C., 2023. Numerical simulation of scour at the rear side of a coastal revetment. Ocean Engineering 275, 114092. doi:10.1016/j.oceaneng.2023.114092.

Speziale, C.G., Sarkar, S., Gatski, T.B., 1991. Modelling the pressure–strain correlation of turbulence: an invariant dynamical systems approach. Journal of Fluid Mechanics 227, 245–272. doi:10.1017/S0022112091000101.

Sun, J., Zou, L., Govender, N., Martínez-Estévez, I., Crespo, A.J., Sun, Z., Domínguez, J.M., 2023. A resolved SPH-DEM coupling method for analysing the interaction of polyhedral granular materials with fluid. Ocean Engineering 287, 115938. doi:10.1016/j.oceaneng.2023.115938.

Sun, J.Z., Zou, L., Govender, N., Sun, Z., Yu, Z.B., Jin, G.Q., 2024. Coupling SPH-DEM method for simulating the dynamic response of breakwater structures under severe free surface flow. Powder Technology 441, 119805. doi:10.1016/j.powtec.2024.119805.

USACE, 2002. Coastal engineering manual. Number 1110-2-1100 in Engineer Manual. us army corps of engineers ed., Washington, D.C.

Van Der Meer, J.W., 1987. Stability of breakwater armour layers — design formulae. Coastal Engineering 11, 219–239. doi:10.1016/0378-3839(87)90013-5.

Van Der Meer, J.W., 1988. Deterministic and Probabilistic Design of Breakwater Armor Layers. Journal of Waterway, Port, Coastal, and Ocean Engineering 114, 66–80. doi:10.1061/(ASCE)0733-950X(1988)114:1(66).

Van Gent, M.R.A., Smale, A.J., Kuiper, C., 2004. Stability of Rock Slopes with Shallow Foreshores, in: Coastal Structures 2003, American Society of Civil Engineers, Portland, Oregon, United States. pp. 100–112. doi:10.1061/40733(147)9.

Wachs, A., Girolami, L., Vinay, G., Ferrer, G., 2012. Grains3D, a flexible DEM approach for particles of arbitrary convex shape — Part I: Numerical model and validations. Powder Technology 224, 374–389. doi:10.1016/j.powtec.2012.03.023.

Wang, P., Ji, C., Sun, X., Xu, D., Ying, C., 2024. Development and test of FDEM–FLOW-3D—A CFD–DEM model for the fluid–structure interaction of AccropodeTM blocks under wave loads. Ocean Engineering 303, 117735. doi:10.1016/j.oceaneng.2024.117735.

Wu, K., Yang, D., Wright, N., Khan, A., 2018. An integrated particle model for fluid–particle–structure interaction problems with free-surface flow and structural failure. Journal of Fluids and Structures 76, 166–184. doi:10.1016/j.jfluidstructs.2017.09.011.

Wu, Y.T., Yeh, C.L., Hsiao, S.C., 2014. Three-dimensional numerical simulation on the interaction of solitary waves and porous breakwaters. Coastal Engineering 85, 12–29. doi:10.1016/j.coastaleng.2013.12.003.

Yoon, H.S., Kim, H.l., Yu, H.W., Kim, M.S., 2020. Estimation of Limiting Wave Height for Wave Dissipation Block (Tetrapod) in Busan Coast. Journal of the Korean Society for Marine Environment & Energy 23, 117–125. doi:10.7846/JKOSMEE.2020.23.3.117.

Yu, S., Ransley, E., Qian, L., Zhou, Y., Brown, S., Greaves, D., Hann, M., Holcombe, A., Edwards, E., Tosdevin, T., Jagdale, S., Li, Q., Zhang, Y., Zhang, N., Yan, S., Ma, Q., Tagliafierro, B., Capasso, S., Martínez-Estévez, I., Göteman, M., Bernhoff, H., Karimirad, M., Domínguez, J.M.,

Altomare, C., Viccione, G., Crespo, A.J., Goméz-Gesteira, M., Eskilsson, C., Fernandez, G.V., Andersen, J., Palm, J., Niosi, F., Dell'Edera, O., Sirigu, M., Ghigo, A., Bracco, G., Cui, F., Chen, S., Wang, W., Zhuo, Y., Li, Y., Peyrard, C., Benguigui, W., Barcet, M., Robaux, F., Benoit, M., Teles, M., Ntouras, D., Manolas, D., Papadakis, G., Riziotis, V., Zheng, Z., Lei, W., Wang, R., Chen, J., Shao, Y., Visbech, J., Bingham, H.B., Engsig-Karup, A.P., Zhou, Y., Cai, Y., Zhao, H., Shi, W., Li, X., Zeng, X., Xue, Y., Zhuang, T., Wan, D., Engel, G., Tierno, M., Ducrozet, G., Bouscasse, B., Leroy, V., Ferrant, P., Barajas, G., Lara, J.L., 2025. Modelling the hydrodynamic response of a floating offshore wind turbine – a comparative study. Applied Ocean Research 155, 104441. doi:10.1016/j.apor.2025.104441.

Zhao, X., Hu, C., 2012. Numerical and experimental study on a 2-D floating body under extreme wave conditions. Applied Ocean Research 35, 1–13. doi:10.1016/j.apor.2012.01.001.

Zhao, X., Ye, Z., Fu, Y., Cao, F., 2014. A CIP-based numerical simulation of freak wave impact on a floating body. Ocean Engineering 87, 50–63. doi:10.1016/j.oceaneng.2014.05.009.

Appendix A. Validation of the coupling: sphere bouncing on a plate in a viscous fluid

The goal of this appendix is to validate the DEM-CFD coupling by reproducing the experimental work of Gondret et al. (2002). The experiment consists in studying the rebound of different spheres immersed in various fluids. It allows the deduction of the coefficient of restitution e which mainly depends on the Stokes number St. The dry coefficient of restitution is the ratio of the velocities of the sphere just before and after impact (U_b and U_a, respectively) as measured in air, $e = \frac{U_a}{U_b}$.

One case is presented here with the sedimentation of a 3 mm steel sphere in silicon oil RV10. The container is a vertical tank of dimension 10×10×30 cm, with glass walls and a glass bottom with a roughness of less than 0.2 µm. The sphere is released by magnetic devices just below the air-liquid surface to avoid air entrainment. The precise release height is not specified but the sphere reaches its terminal velocity before the impact, the sphere being released without initial rotational or translational velocity. The Stokes number, comparing the spheres inertia relative to the viscous force is here defined as

$$St = \frac{2}{9}\frac{\rho_s U R}{\mu} = \frac{1}{9}\frac{\rho_s}{\rho_f} Re \tag{22}$$

with ρ_s and ρ_f the solid and fluid densities, respectively, U the particle velocity, R the particle radius, μ the dynamic viscosity of the fluid and Re the Reynolds number. In this case, the silicon oil RV10 has a density of $\rho_f = 935\,\mathrm{kg/m^3}$ and a dynamic viscosity of $\nu = 10 \times 10^{-3}\,\mathrm{Pa \cdot s}$, which is approximately 10 times larger than water. The density of the steel sphere is $\rho_s = 7800\,\mathrm{kg/m^3}$ and the dry coefficient of restitution experimentally measured is $e = 0.97 \pm 0.01$.

Numerically, the tank is reproduced with a cartesian mesh, with wall boundaries for the bottom plate and for the four sides. The top boundary is an output located 5 cm above the free surface with a fixed mean pressure at standard atmospheric condition. In order to limit the size of the mesh, only the central column of the tank is taken into account with a size of 10 sphere diameters. The grid size is determined so that the diameter of the sphere is slightly bigger than 10 cells, which was determined based on a mesh sensitivity study. Furthermore, a specific refinement is performed close to the bottom boundary. In the fluid solver, the sphere is defined using the Time and Space Dependant Porosity method. The diameter used in the fluid solver is the same as the real diameter. On the other hand, the diameter used in the DEM solver is taken larger than the real diameter in order to avoid the presence of two walls inside a cell, when the object is re-constructed in the fluid solver. The sphere density in the DEM solver is then recalculated so that the mass remains constant. Three diameters are tested, with enlargements of 2%, 5% and 10%.

The results are shown Figure 17 with the comparison between the experimental and numerical studies. The first verification to be made is that the terminal velocity reached before impact is correctly predicted, as it can be verified in Figure 17b. Then, rebound heights and velocities can be observed, with some slight differences: four rebounds are experimentally observed before the sphere settles down. On the other hand, the simulations show many more bounces whose amplitude slowly decreases before eventually stopping. This difference comes from two factors: the space artificially left between the plate and the sphere, and the lack of lubrication force in the model. The lower the Stokes number is, the more these effects will be visible. For coastal applications, the Stokes number is in general much larger than unity so the present approach is suitable for describing solid-solid interactions. Regarding the impact of the size of the DEM sphere compared to the original size of the sphere, it can be seen that the results are similar. The sphere with the highest ratio of 10% shows higher bounces once the third bounce reached, as walls effect have less impact the wider the gap is. It is important to highlight that these results are obtained for normal impacts and with a high Stokes number, therefore with few lubrication effects at stakes.

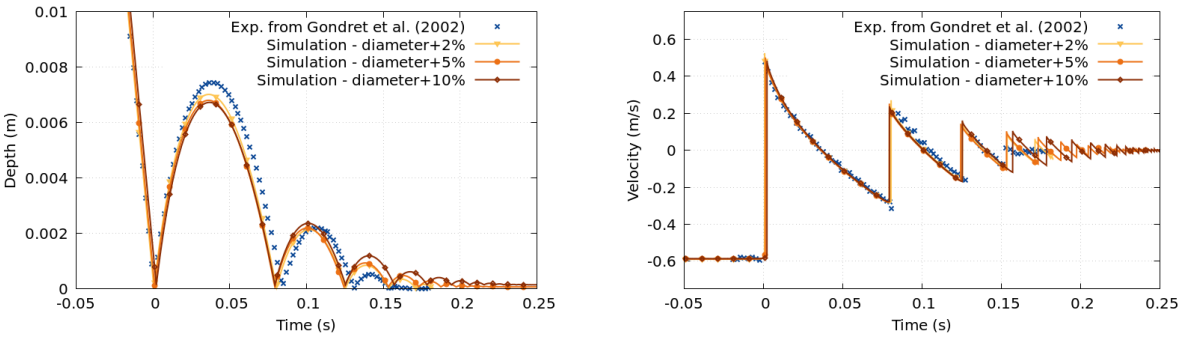

Figure 17: Displacement (a) and velocity (b) of a 3 mm steel sphere in silicon oil RV10

Appendix B. Tetrapod geometrical definition and mesh sensitivity analysis

The information given by Mitsui et al. (2023) on the geometrical definition of the tetrapods used during the experiments are their height (7.7 cm), volume (126 cm^3) and mass (0.3 kg), as well as a scale factor to a prototype tetrapod (1:50). However, these information are not enough to model a realistic tetrapod. Using characteristic dimensions of tetrapods given by Yoon et al. (2020) based on data from KPHA (Korea Ports and Harbours Association), realistic geometrical parameters were determined. The geometry is then simplified to be represented with four truncated cones and one central sphere. As the real and modeled geometries are different, some parameters have to be (slightly) adapted to fit the requirements, as presented in Figure 18.

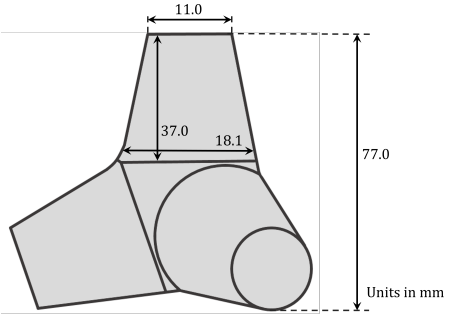

Figure 18: Dimensions of the tetrapod used in the simulations.

Once the geometry is defined, the volume and the mass can be deduced by numerical integration. This integration is done by creating a very fine 3D mesh around the object and then summing the volumes of the elementary cubes which have their centers inside the tetrapod. The comparison of the geometrical parameters between the original tetrapod, the scale model from Mitsui et al. (2023) and the present simplified scale model is presented in table 4.

As presented in section 2, a gap has to be left between the DEM boundary geometrical definition and the discrete forcing boundary to enable the discrete forcing reconstruction at the interface between two objects. In this specific case, it was chosen to keep the discrete forcing boundary at its original size and to enlarge the DEM object, as the interactions between tetrapods are limited and as the movement is mainly governed by the fluid-structure interactions. The radius of the arms of the tetrapods are therefore increase by 2 mm and their height by 5 mm, leaving a gap between the mound and the tetrapods of about 3 mm, slightly superior to the mesh base size which is 2.5 mm. Furthermore, a sublayer is added to the mesh between the tetrapod and the mound to improve its resolution. The masses and inertias are kept to their original values.

A mesh sensitivity analysis is performed prior to the full scale simulation. Preliminary simulations show that the tetrapods sustain fluid forces of approximately 1.2 N for the strongest wave case. The sensitivity study is then performed with a dam break simulation yielding a force of this order of magnitude. The sensitivity analysis is performed regarding

Table 4: Parameters comparison between the real tetrapod block, the present geometrically simplified block at 1:50 scale and the block used by Mitsui et al. (2023).

	40 t - Yoon et al.	Present 1:50 scale	Mitsui et al.
Height	3.860 m	77.0 mm	77 mm
Volume	16 m^3	125.91 cm^3	126 cm^3
Mass	36.80 t	299.68 g	300 g
Density	2.3 t/m^3	2.38 g/cm^3	2.38 g/cm^3

the final displacement of the tetrapod following the passage of the water initially contained in the tank and is presented in Figure 19. As a result, a mesh size corresponding to 32 cells per tetrapod height is chosen for the simulations (i.e. 2.5 mm). Furthermore, a sensitivity analysis to the size of the DEM boundary is also performed on the chosen mesh. Two other tetrapod sizes are evaluated: one with an increase of 5% and one with an increase of 10% relative to the DEM size used in the simulations. It can be seen that the increase of 5% has a moderate impact on the results while the 10% increase gives substantially different results. The convergence supports the idea that the increase in size is sufficiently moderate to give reliable results.

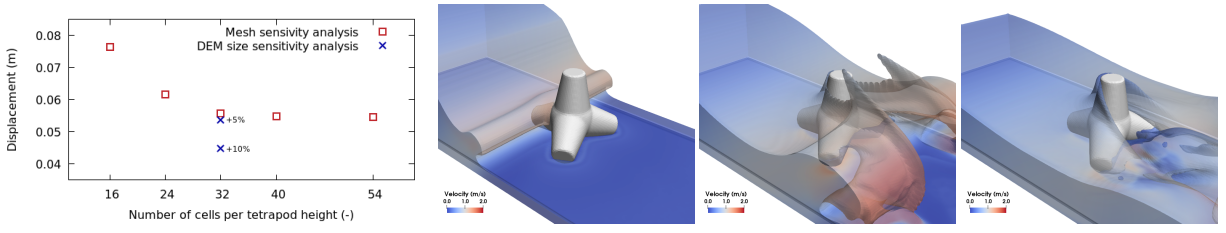

Figure 19: Mesh sensitivity analysis performed on the problem of an armour blocks displaced by a water dam-break: (a) maximum displacement of the block as a function of the mesh size, and sensitivity analysis to the DEM size of the tetrapod; (b, c, d) Snapshots of the free-surface and the tetrapod at increasing time instants.

Appendix C. Mesh sensitivity analysis for the wave forces on a idealised breakwater

A mesh sensitivity analysis is performed on the case W2 of the idealised breakwater case. The results are presented in Figure 20 and show that a mesh base size of $\Delta x = 0.050$ m is sufficient to capture the forces. With this mesh refinement, one sphere diameter corresponds to 20 cells.

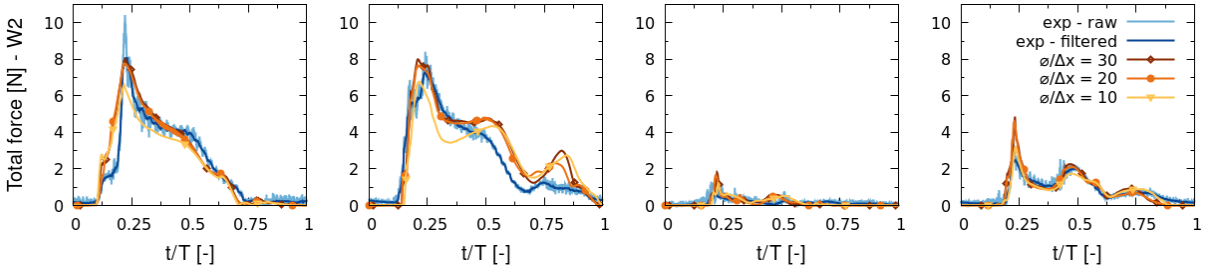

Figure 20: Total phase averaged fluid forces applied on the spheres for the case W2. Experimental signals are presented raw and filtered, numerical signals are presented with 3 different levels of refinement, with respectively 10, 20 and 30 cells in one sphere diameter.

Table 5: Computation characteristics of simulations presented in sections 3 and 4.

Case	Idealised breakwater	Wave impact on tetrapods
Number of cells	6.6×10^6	12.6×10^6
Number of nodes	10	15
Number of cores	480	720
Computation time (h)	30	30

Appendix D. Computing statistics

Simulations of both section 3 and section 4 were performed using EDF supercomputer Cronos, with 2nd Gen Intel Xeon Platinum 8260 processors at 2.40 GHz, with 192 Go of RAM. For section 3, the results indicated in table 5 correspond to about 10 s of physical time at model's scale (between 5 and 8 wave periods). For section 4, the results correspond to the passing of a solitary wave, which takes about 20 s of physical time at model's scale.